Angewandte Chemie
Eine Zeitschrift der Gesellschaft Deutscher Chemiker

Supporting Information

Autocatalytic Nucleation and Self-Assembly of Inorganic Nanoparticles into Complex Biosimilar Networks

*C. N. McGlothin, K. G. Whisnant, E. S. Turali Emre, D. Owuor, J. Lu, X. Xiao, D. Vecchio, S. Van Epps, P. Bogdan, N. Kotov**

Supplementary Information

Autocatalytic Nucleation and Self-Assembly of Inorganic Nanoparticles into Complex Biosimilar Networks

Connor N. McGlothin[1,2,3], Kody G. Whisnant[1,2,3], Emine Sumeyra Turali Emre[1,2,3], Dickson Owuor[1,2,3,4], Jun Lu[1,2,3], Xiongye Xiao,[1,5] Drew Vecchio,[1,2] Scott VanEpps[2,6], Paul Bogdan,[1,5] Nicholas A. Kotov[1,2,3,6*]

[1] Center of Complex Particle Systems (COMPASS), University of Michigan, Ann Arbor, MI, USA;

[2] Biointerfaces Institute, University of Michigan; Ann Arbor, 48109, USA;

[3] Department of Chemical Engineering, University of Michigan; Ann Arbor, Michigan 48109, USA;

[4] Strathmore University, Madaraka Estate, Nairobi, Kenya;

[5] Ming Hsieh Department of Electrical and Computer Engineering, University of Southern California, Los Angeles, CA 90007 USA;

[6] Department of Emergency Medicine, University of Michigan; Ann Arbor, 48109, USA;

This file includes:

Additional Materials
Additional Methods
Supplementary Comments 1 to 11
Supplementary Figs. S1 to S19
Legends for Movies S1 to S4

Materials and Methods

Chemicals

Silver nitrate ($AgNO_3$, ≥99.0%, Cat.# 209139), sodium citrate dihydrate (citrate, ≥99.0%, Cat.# S4641), sodium hydroxide (NaOH, ≥98%, Cat.# S5881), poly(diallyldimethylammonium chloride) (PDDA, MW~200,000-350,000, 20 wt% in water, Cat.# 409022), poly(sodium 4-sytrenesulfonate) (PSS, MW~70,000, Cat.# 243051), acetic acid (99.8-100.5%, Cat.# 27225), ammonia solution (28% in water, ≥99.99%, Cat.# 338818), and hydrazine hydrate (50-60% in water, Cat.# 225819) were all purchased from Sigma-Aldrich. Isopropanol (≥99.9%, Cat. # A451-4) was purchased from Thermo Fisher Scientific. Millipore water from a Direct-Q3 water purification system (18.2 MΩcm, Millipore) was used for this work.

Media and light conditions for self-replication and self-assembly of nanoparticles (NPs)

Silver NPs were synthesized through a photoinduced reaction with illumination by an 8 W 365 nm ultraviolet (UV) portable lamp (Analytik Jena). For most experiments, 3 mM citrate and 0.1 mM $AgNO_3$ were mixed in 50 mL of water. 0.1 M NaOH was added dropwise to the solution while stirring until the solution reached pH 10.3. The concentration of the silver precursor was chosen so that its plasmonic band does not saturate the UV-Vis spectrometer throughout the entire synthesis. Media with pH above 10.3 leads to formation of silver oxide/hydroxide particles, which leads to a chemical system with a greater number of components and stronger light scattering. It is also suitable for the study of self-replication and self-assembly processes, but the dispersions with these new NPs require a larger number of parameters, such as thermodynamic characteristics of both silver oxide and hydroxide (see Eq. S12).

The solution was placed in an ice bath and dark environment to maintain a constant temperature of 3-5 ^{o}C throughout the synthesis while eliminating any thermodynamic effects caused by heating from the light source and to eliminate ambient light effects, respectively. The solution is illuminated with the UV lamp with maximum emission wavelength at 365 nm for up to 180 min (3 hours) while constantly agitated with a 2.5 cm stir bar rotating at 350 rpm.

Aliquots of the solution were taken at various time points during the synthesis and characterised immediately under ultraviolet-visible (UV-Vis) spectroscopy to ensure no precipitation of silver oxide (Ag_2O) occurred. For experiments with the 8 W lamp, the light intensity at the solution was 1.3 mW/cm^2. For the higher intensity light experiments, a 100 W high intensity portable UV lamp (Analytik Jena) with a maximum emission wavelength at 365 nm was used and the distance between the solution and light was adjusted for the other two light intensities used in this study (8 and 17.2 mW/cm^2).

Measurements of NP concentration

For preliminary screening, an Agilent 8453 UV-Vis spectrometer was used to analyse the extinction spectra of the NP solutions at various times through the synthesis. 530 µL aliquots were taken from the solution at varying time points (e.g., every 10, 15, and 30 min) and deposited into a micro spectrophotometer cell (Starna Cells) for analysis. The plasmonic peak of the NPs measured from 400 to 420 nm during the synthesis, with a Gaussian distribution roughly between 325 nm and 500 nm, was further used for the analysis.

The concentration of NPs was measured using a Malvern Nanosight NS300 and NP tracking analysis (NTA). For NTA, a 405 nm laser module was used to track the number of NPs. The 405 nm laser is within the absorbance range of the NPs and as a result, led to visually observable new NP nucleation when viewing the solution under the laser module. To counteract unintended nucleation, 0.1 mM NaCl was mixed in the sample aliquot to prevent further formation of NPs during analysis. Any unreacted Ag^+ ions in the solution reacted with NaCl and precipitated as AgCl. The solution was centrifuged at 2,500 rpm for 10 minutes in an Eppendorf 5417R to separate the larger AgCl particles from the sample. UV-Vis spectroscopy was used to test the colloidal stability of NP dispersions under 0.1 mM NaCl. The UV-Vis spectra of NP dispersions do not change with NaCl concentration, characteristic of NTA conditions. NTA was run five times to acquire data sufficient for representative statistical analysis and accurate error assessment.

TEM imaging

TEM imaging was performed on a Thermo Fisher Talos F200X G2 scanning transmission electron microscope (S/TEM) with a 200 kV accelerating voltage. TEM samples were prepared by drop casting 4 μL of solution on a 400-mesh copper grid with an ultrathin carbon film on lacey carbon support film (Ted Pella, Cat. # 01824) after centrifuging the solution at 12,500 rpm for 30 minutes to remove unreacted Ag^+ ions and residual citrate and washed with ultrapure water. The TEM sample was allowed to air dry over night before being imaged.

Dark-field microscopy for observing formation of NP self-replication coupled with self-assembly

Dark-field microscopy was performed using an Olympus IX81 inverted microscope equipped with an Olympus U-DCW dark-field oil-immersion objective (NA 1.2-1.4). The scattered light was captured through a 60x dry objective (NA 0.9, Olympus) and imaged through an electron-multiplying charged-coupled device (EMCCD) camera (Andor IXon Ultra). The solution was imaged between a glass slide and a cover slip with cover slip spacers to allow a small gap to fill up with the unreacted self-replicating solution. The solution was sealed using bee wax to ensure no evaporation leading to false Brownian motion and unwanted flow under imaging. The 8W 365nm UV light was illuminated on the sample during the imaging to allow synthesis of the NPs while imaging.

Layer-by-layer functionalized TEM grids

TEM grids were functionalized by $(PDDA/PSS)_3PDDA$ multilayers prepared following the standard layer-by-layer (LBL) processing protocol.[1] Multilayer architechture with the final layer being positively charged were used to capture NPs as they self-replicate and self-assemble under 2D constrains on the solid surfaces. Specifically, the LBL deposition was performed first with PDDA where the TEM grid or other substrates were submerged in a 1 wt% aqueous solution of PDDA for 10 minutes. Then, the TEM grid was removed and washed three times with water to remove any residual PDDA solution. The grid is air dried and then submerged in a 1 wt% aqueous solution of PSS for 10 minutes. The grid was again washed 3 times with water and allowed to air dry. This process was repeated to create 3 bilayers to ensure a uniform coating. One more layer of PDDA was applied to leave the surface positively charged to attract the negatively charged NPs. The functionalized TEM grid was dipped in the reaction solution at the inflection point of the synthesis (60 min), where there should be the maximum rate of self-replication and the most NP

assemblies, and immediately removed to prevent any additional nucleation on the grid. The TEM grid was washed with water three times to remove any residual reaction solution and left only the moment-in-time capture of the assemblies. The grid was air dried, and the assemblies were then imaged under TEM.

Cryo-TEM for moment-in-time experiments

Cryo-TEM was performed on a Thermo Fisher Talos F200X G2 scanning transmission electron microscope (S/TEM) with a 200 kV accelerating voltage. An aliquot of the reaction solution was taken at the inflection point (60 min) of the synthesis where the most self-replication is occurring. The solution was immediately drop-casted onto a TEM grid and blotted using filter paper to create a thin enough liquid layer for viewing under TEM. The grid was then instantly vitrified by submerging it in liquid ethane followed by submerging the grid in liquid nitrogen. The frozen TEM grid was setup in a Gatan Elsa cryo-transfer holder that is specialized for cryo-TEM and imaged.

In situ Liquid TEM

In situ TEM was performed on a Thermo Fisher Talos F200X G2 scanning transmission electron microscope (S/TEM) with a 200 kV accelerating voltage. A viewing cell (Hummingbird Scientific) consisting of two silicon chips with transparent silicon nitride windows separated by a 100 nm spacer were used. The viewing cell chips were plasma cleaned to create a hydrophilic surface for better flow and dispersion of the solution in the holder. A liquid cell TEM holder (Hummingbird Scientific) was assembled with the silicon chips and placed in a pumping station (Hummingbird Scientific) to ensure that the holder maintains its integrity under vacuum before being placed in the TEM. The self-replicating solution was pumped through the holder, and the liquid cell holder was placed in the TEM equipment and aligned to view the sample. Electron dose rate is kept at or below 130 e^-/Å·s to allow for self-replication without other species forming. To view the nuclei forming at the interface of parent NPs, the electron dose rate was increased above 200 e^-/Å·s to destabilize the nuclei to view them (**Movie S3**).

Kinetic model

The kinetic model is a modification of the Finke-Watzky model, which is a two-step simplified model of NP nucleation and autocatalytic growth (*32*):

$$A \xrightarrow{k_1} B \qquad \text{(Eq. S1)}$$

$$A + B \xrightarrow{k_2} 2B \qquad \text{(Eq. S2)}$$

Here, A is the precursor which in this case is Ag^+ ions and B is Ag^0 atoms in the NPs. The first equation is the reduction of silver ions to silver NPs. The second equation is the autocatalytic growth of the silver NPs. Our kinetic model follows this mechanism but is first modified to include only autocatalytic growth on the surface of the NPs. Our model also incorporates a third equation, which is the self-replicating equation where the fully grown NPs induce the nucleation of silver nuclei at a rate faster than the first equation. Full explanation of the kinetic model can be seen in

Supplementary Text 9,
Assesment of the Fink-Watzky model to describe the experimental accumulation kinetics for self-replicating NPs.

LBL deposition of PDDA and PSS were performed on silicon monoxide (SiO) TEM grids and glass coverslips following the method described above to produce multilayers with the cumulative film sequence $(PDDA/PSS)_3PDDA$. The substrates were washed with water to remove any excess polymers and dried at room temperature. The substrates were then supported on the surface of the solution at the inflection point of the synthesis (60 min) to allow only growth on the submerged side. This is done to avoid any attenuation through the solution as more NPs form if the substrate is completely submerged. The substrate is then removed from the surface of the solution after 30 min when formation of new NPs significantly decreases. The substrate is washed with water and allowed to air dry before being characterised.

ZnO/Fe_2O_3 HPs were synthesized using a method developed previously in our lab.[2] The HPs were dispersed in the reaction solution at the inflection point of the synthesis (60 min) and stirred for 30 min while still under illumination. The solution was centrifuged at 4000 rpm for 20 min to separate the HPs from the smaller NPs. The HPs were redispersed in water and then drop cast on a silicon wafer for imaging.

Electroless silver deposition onto self-replicated networks

The deposition solution is based on a Tollen's reagent, which consists of two solutions. The first solution consists of 20 mM $AgNO_3$, 8.8 mL isopropanol, 1.2 mL acetic acid, and 40 mL 25% ammonia solution. The second solution consists of 0.5 mL hydrazine and 49.5 mL isopropanol. 7.5 mL of each solution is added to 15 mL of water while stirring to create the Tollen's reagent. Due to the short shelf life of the reagent, it must be prepared fresh each day it is used. The desired substrate is submerged in the deposition solution for 5 to 40 min depending on the desired amount of silver to be deposited. The substrate is then removed from the solution and washed 3 times with water. The substrate is air dried before any characterisation.

Imaging of NP networks

Scanning electron microscopy (SEM) images were acquired using a Thermo Fisher Helios 650 Nanolab at 3 kV accelerating voltage and 0.1 nA beam current. Samples that were prepared with electroless silver deposition seen above were placed in the SEM equipment for viewing.

Measuring sheet resistance of NP networks on solid substrates

A four-point probe (Signatone SP4) powered by a source meter (Keithley Model 2470) is used to measure the sheet resistance of our silver thin films. A current of 1 mA was applied and the voltage was measured. The sheet resistance was calculated using Eq. S3:

$$R_S = \frac{\pi}{\ln(2)}\frac{\Delta V}{I} = 4.53\frac{\Delta V}{I} \qquad \text{(Eq. S3)}$$

Where R_S is the sheet resistance in Ω/sq, ΔV is the change in voltage (mV) measured between the two inner probes, and I is the current (mA) applied between the outer probes.

Imaging of Bacterial Networks

Many bacteria form chains as they replicate. This process is particularly well-known for *Streptococcus spp*. and, specifically for *Streptococcus pyogenes* (*S. pyogenes*) that causes common pyogenic infections, exemplified by pharyngitis, cellulitis, impetigo, and erysipelas. They are also involved in toxigenic infections, such as the infamous necrotizing fasciitis.

We used *Streptococcus spp.* strain from a glycerol stock of a patient sample collected from an endotracheal tube. The bacteria were cultured on tryptic soy agar at 37 °C for 18 hours. From the agar plate, we selected a single colony of bacteria and inoculated it into tryptic soy broth enriched with glucose. The inoculum was then incubated at 37 °C with constant shaking until it reached mid-logarithmic phase with a plate count of 0.4. To induce chain formation, we added 100 µL of bacterial culture to tissue culture-treated glass slides (Ibidi USA 80136) and allowed it to settle at the bottom for an hour before adding 1 mL media. We then placed the dish in a BD GasPak™ EZ container system (BD 260679) to help generate anaerobic, CO_2-enriched environments for three days at 37 °C, changing the medium daily. During this period, we monitored the formation of chains using gram-negative staining and light microscopy.

After the induction period, the formed biofilm samples were fixed in a solution containing 2.5% glutaraldehyde in 0.1 M phosphate buffer for 16 hours at 4 °C. We then washed the bacterial samples with phosphate buffer and dehydrated them using a series of ethanol solutions in water with concentrations of 30%, 50%, 70%, 90%, 95%, and 100% ethanol. The dehydrated biofilm samples were mounted on SEM stubs using conductive adhesive tabs. We sputter-coated the samples with a thin layer of gold to enhance conductivity and prevent charging during SEM imaging. Finally, the coated bacterial samples were imaged using a FEI Helios 650 Nanolab at an accelerating voltage of 1 kV. We captured images at various magnifications to visualize the morphology and network arrangement of the chain-forming Streptococcus bacteria.

Imaging of Fungal Networks

The fungal networks were grown on segments of tissues of green peppers, *Capsicum annuum L*, following the standard protocol.[3] Specifically, the sections of *Capsicum annuum L* were placed in individual plastic bags for humidity control. The samples were incubated at 25 °C for 5 days specific for the rapid proliferation of *R. stolonifera*. After the incubation period, we collected representative slices and examined them under a light microscope (Nikon Microscope with Scion CCD Camera) confirming the morphology of the growing fungal networks as *R. stolonifera*. Based on our initial observation, the fungal network species was cottony in appearance, which is typically associated with its hyphal structure. The morphological features of *R. stolonifera* matched perfectly with the structure of the fungi species including a body containing branched mycelium and a coenocytic network structure. The microscopic images for subsequent GT calculations using *StructuralGT* were processed by ImageJ software (https://imagej.net/), adjusting contrast and brightness to enhance the clarity of the image based on NIH-approved protocols.

SUPPLEMENTARY TEXTS

Supplementary Text 1: Analysis of the UV-Vis spectral features and nucleation kinetics

A solution of 0.1 mM silver nitrate ($AgNO_3$) and 3 mM sodium citrate dihydrate (citrate) at a critical pH of 10.3 was illuminated under 365 nm UV light with an intensity of 1.3 mW/cm^2 to induce NP nucleation and self-replication. The concentration of the silver precursor was chosen so that the final concentration of plasmonic NPs did not saturate the UV-Vis spectrometer throughout the synthesis. The UV-Vis spectrum was obtained for wavelengths from 190 to 1100 nm. Only two peaks were observed (**fig. S1A**). The peak around 400 to 420 nm is the plasmonic peak of the spherical NPs, while the peak at 200 nm is from the citrate in the solution. The max wavelength was observed to shift slightly to a higher wavelength, but then steadily blue-shifted down to 403 nm at 180 min (**fig. S1B**).

The kinetic curve of the extinction intensity over time (**Fig. 1B**) displayed three distinct features:[4] (**1**) a slow initial homogeneous nucleation over the first 30 min; (**2**) an increase in nucleation rate as the initial NPs begin to self-replicate; and (**3**) a decrease in the rate of nucleation at 150 min upon depletion of the silver precursor.

Supplementary Text 2: Effects of pH

Various pH levels were tested for the self-replication conditions. The extinction intensity at maximal wavelength was measured at 30 min intervals up to 180 min, where pH 10.3 goes to completion (**fig. S2**). At pH 10.3, there is an incubation period up to 30 min where homogeneous nucleation of NPs is occuring slowly, followed by a rapid increase in extinction intensity up to 150 min as heterogeneous self-replication is occuring, leading to an S-shape curve in extinction over time. At pH 9.5, it is observed that there is a similar incubation period as that at pH 10.3, but it is followed by a linear increase in extinction intensity after 30 min. A similar trend for pH 9.5 can be seen for pH 8.3, but at a slower rate of nucleation. A pH of 8.3 is the initial pH of the as-made dispersion without any addition of NaOH or other base.

Supplementary Text 3: Blue-shift in extinction peak over time

On average, as the NPs increase in size throughout the synthesis, one would expect to see effects on the extinction intensity of the solution as larger particles will scatter more light and will also lead to shifts of higher max extinction wavelengths. Interestingly, the plasmonic peak shifts to a lower wavelength, or blue-shifts (**fig. S1B**), which is in contradiction to what one would expect for plasmonic NPs as they increase in size. The blue shift can be attributed to the change in charge density around the NPs (**fig. S4**). As a result, extinction is not perfectly correlated to the NP concentration but is still good for preliminary screening of self-replicating capabilities.

To account for the blue-shift in max wavelength over the course of the synthesis, a post synthesis technique was used. The solution of NPs, after 180 min of reaction time, were analysed using UV-Vis spectroscopy, and the max wavelength is 405 nm (**fig. S4A**). 0.1 mM $AgNO_3$ was added to the post-synthesis solution and the extinction spectrum was measured. No shift in the max wavelength was observed. The solution was then exposed under 365 nm UV light for 10 min to "reactivate" the self-replicating NPs. The extinction spectrum is seen to red-shift to 411 nm as the silver ions start to reduce to silver atoms in the electron double-layer of the NPs, leading to a lower electron density of the NPs. This decrease in electron density is what leads to the red-shift

in wavelength. To further confirm that the electron density changes cause the max wavelength shifts, the "reactivated" solution of NPs was centrifuged at 12,500 rpm for 20 min to remove any excess silver ions in solution and the solution was redispersed in a 3 mM citrate solution to maintain similar conditions to the 180 min post-synthesis solution. Max wavelength of the redispersed solution remained at 411 nm. Finally, the redispersed solution was exposed to UV light for 15 min to react any residual silver ions within the electron double-layer of the NPs. As one would expect, the max wavelength shifts back to 405 nm, similar to that of the post-synthesis solution. This is due to an increase in the electron density of the NPs as there were no more silver ions to reduce in the electron double-layer. TEM images of the NPs at the start of this technique were taken to show that there is no size change throughout the process that could have led to any wavelength shifts (**fig. S4B**).

Supplementary Text 4: Zeta-potential

The post-synthesis zeta-potential of the solution was analyzed using a Malvern Zetasizer Nano ZSP. The distribution was fairly large as seen in **fig. S5A**. The average zeta potential was -31.7±32.0 mV. To check whether this is a common surface charge for NPs of our size, which is roughly 14-18 nm, 20 nm citrate-stabilized NPs were purchased from Sigma-Aldrich (0.02 mg/mL in aqueous citrate buffer, Cat.# 730793). Examining the zeta-potential of the solution, the distribution of surface charge was larger than that of the purchased silver NPs. The zeta-potential distribution of these monodisperse 20 nm NPs was more narrow and had an average potential of -38.8 ± 12.1 mV (**fig. S5B**). This difference in distribution, but similar average potential, indicates that there are more complex structures within our system, which is further analyzed in the main text.

Supplementary Text 5: Dark-field microscopy

Dark-field microscopy was used as a preliminary method to view the synthesis of the NPs in real time (**fig. S6A** and **Movie S1**). Particle nucleation starts off slowly until 45 seconds into the synthesis, when nucleation starts to rapidly increase. Some particles can be seen at time 0 as the light source is needed to focus the microscope before the synthesis begins, which is unavoidable. The count of NPs indicates an S-shaped curve over time until the viewing screen reaches saturation. Another important discovery from this microscopy is that, upon zooming in on the synthesis at multiple points, we observed chain-like assemblies of the NPs (**fig. S6C**).

Supplementary Text 6: Moment-in-time capture of chain assemblies

TEM grids were functionalized with $(PDDA/PSS)_3PDDA$ multilayers. The purpose of this method was to prevent any drying effects on the TEM grid and capture the interaction between NPs as they continue to self-replicate. The positive charge of the final PDDA layer attracts the negatively charged NPs to its surface when it is submerged in the illuminated solution. Various NP chain-lengths as they are self-replicating can be seen when captured on the LBL-functionalized TEM grids at the 60 min point of the synthesis (**fig. S8**).

Supplementary Text 7: Liquid phase TEM (LPTEM) at high electron dose rates

The self-replication coupled to self-assembly under light and under electron beam are nearly identical processes because they are both based on solvated electrons whose formation is

promoted by NPs. As expected, the rate of electron generated NPs under electron beam is higher than under light and is dependent on the electron dose rate. Typically, in our imaging LPTEM experiments, the electron dose rate was kept at or below 130 e^-/Å·s when viewing the self-replication of the NPs (**Movie S2**). This dose rate was chosen to balance the stability of the NP formation with the resolution of the TEM imaging.

As the NPs self-replicate, it is possible to observe the initial stages of the critical nuclei formation at the interface of another NP as it occurs faster than the frame rate of the TEM camera. Also, a dose rate well above 130 e^-/Å·s can lead to some instability of the NPs and especially the nuclei forming at the interface of the parent particles. Allowing some NPs to self-replicate initially at 130 e^-/Å·s and then increasing the electron dose rate to 200 e^-/Å·s led to destabilization of any new nuclei that formed at the interface and prevented them from growing into NPs. This lack of stability allowed us to view the initial nucleation and analyse the diameter of the initial nuclei (**Movie S3**).

Supplementary Text 8: LPTEM under non self-replicating conditions (control experiments)

As a benchmark experiment, we tested the dynamics and localization of NPs at conditions where an S-curve was not seen by UV-Vis spectroscopy, NTA, dark field microscopy, and other methods (**Fig. S10** and **Movie S4**). The electron dose rate was kept at 130 e^-/Å·s to maintain the same TEM conditions used for the self-replication system at pH 10.3. NPs were slowly nucleated on the surface of the LPTEM windows, but no self-replication process or axial assemblies were observed.

Supplementary Text 9: Assesment of the Fink-Watzky model to describe the experimental accumulation kinetics for self-replicating NPs.

Based on previous studies of nucleation kinetics,[5] the two-step Finke-Watzky mechanism of NP formation can possibly be an alternative to the set of kinetic equations we utilized in the self-replication model. The suitability of (**fig. S11**) for the description of NP accumulation kinetics in the case of self-replication, can be acessed via calculation of the consecutive time derivatives of the particle concentration [NP], that is, *formation rate, fr* = ($d[NP]/dt$), *acceleration, a* = ($d^2[NP]/dt^2$), and *jerk, j* = ($d^3[NP]/dt^3$), (**figs. S11C, S12, S14)**. These dependences vividly indicate that this potentially plausible model does not really fit the experimental data. Even for the best fit of the Finke-Watzky model to the experimental data in **fig. S11C**, we see dramatic deviations:

(1) For a self-replicating system, one would expect the *formation rate* to start at nearly zero because of the induction period as we observe in the experiment shown in **Fig. 3**. Then *fr* should increase exponentially until it reaches a maximum at which time the rate decreases back to zero. This is not the case for the Finke-Watzky model where the formation rate is finite and high at the onset of the reaction (**fig. S12B**).

(2) *Acceleration* in the self-replicating reaction should display a symmetrical heartbeat-like curve. Considering the rapid accumulation of particles, *a* must quickly rise, starting from zero. This should continue until *a* reaches a maximum corresponding to the end of the induction period. After that, the exponential growth in NPs leads to a rapid decline in acceleration as reactant is being consumed until again a minimum is reached where the reactant concentration, and thus *a*, approaches zero. The Finke-Watzky model pattern is

clearly different (**fig. S12C**) with strong negative peak. Also, the value of *a* never reaches above zero.

(3) *Jerk* of a self-replicating reaction must display two minor positive maxima and a major negative minimum between those two peaks. The zero crossover points correspond to the end of the induction period and the depletion of reactants as observed in the experiment shown in **Fig. 3**. The minimum corresponds to the inflection point in NP accumulation when self-replication is the fastest. The Finke-Watzky model is very different (**fig. S12D**).

Supplementary Text 10: The self-replicating kinetic model

We modified the two-step Finke-Watzky model to include chemical Equations (Eqs.) S4-S6, which are essential for photoinduced autocatalysis described in the schematics of **Fig. 1A**. In these equations, Ag^+ represents the silver ions from the precursor $AgNO_3$. Ag^0 are the solvated silver atoms; they form the core of both NP_d and NP_m. Ag^0_{surf} are the silver atoms coordinated with the NPs with citrate surface ligands. These are the atoms that can be exchanged between NPs as observed in **Fig. 2** and are the atoms that can also capture the photoejected electrons in the post-nucleation growth period. *N* is the total number of both NP_d and NP_d in the system:

$$Ag^+ + e \xrightarrow{k_1} Ag^0 \qquad \text{(Eq. S4)}$$

$$Ag^+ + Ag^0_{surf} + e \xrightarrow{k_2} Ag^0 + Ag^0_{surf} \qquad \text{(Eq. S5)}$$

$$Ag^+ + N + e \xrightarrow{k_3} Ag^0 + N \qquad \text{(Eq. S6)}$$

The rate of electron photoejection, *e*, is in steady state with *de/dt* = 0 because it is determined by the illumination conditions. The differential equations that arise from these chemical equations (Eq. S4-S6) are:

$$\frac{dAg^+}{dt} = -k_1 Ag^+(t) - k_2 Ag^+(t) Ag^0_{surf}(t) - k_3 Ag^+(t) N(t) \qquad \text{(Eq. S7)}$$

$$\frac{dAg^0}{dt} = k_1 Ag^+(t) + k_2 Ag^+(t) Ag^0_{surf}(t) + k_3 Ag^+(t) N(t) \qquad \text{(Eq. S8)}$$

$$\frac{dN}{dt} = \frac{k_1 Ag^+(t) + k_3 Ag^+(t) N(t)}{m} \qquad \text{(Eq. S9)}$$

Here, *m* is the smallest stable cluster of Ag^0, also known as critical nuclei. Based on the data by Völkle, Gebauer, and Cölfen, *m* ~ 30 atoms.[6] The average diameter and total bulk/surface atoms in all NPs over the course of the reaction were calculated as

$$d = \sqrt[3]{\frac{6(Silver\ Atoms\ in\ AgNPs)M_w}{\pi(Number\ of\ AgNPs)\rho N_A}} \quad \text{(Eq. S10)}$$

$$d_{bulk} = d - 4R_{Ag} \quad \text{(Eq. S11)}$$

$$Ag^0_{bulk} = \frac{\pi d^3_{bulk}\rho N_A}{6M_w} N(t) \quad \text{(Eq. S12)}$$

$$Ag^0_{surf} = Ag^0_{tot} - Ag^0_{bulk} \quad \text{(Eq. S13)}$$

where d is the average diameter of the NPs, M_w is the molecular weight of silver (107.868 g/mol), ρ is the density of silver (10.49 g/cm^3), N_A is Avogadro's number, d_{bulk} is the diameter of a NP beneath the surface atoms, R_{Ag} is the radius of a silver atom (0.165 nm), and Ag^0_{bulk} is the total number of atoms in a NP minus the surface atoms. Experimental results were fitted to this model using Matlab and its *lsqcurvefit* function.

Our model resulted in an excellent fit to the NP accumulation curves under variable light intensities of 1.3, 8, and 17.2 mW/cm^2 (**Fig. 3**) and matched the higher temportal derivatives of [NP] in **fig. S12**.

Additional results from this model for other chemical components in Eqs. S4-S6 (Ag^+, Ag^0, Ag^0_{bulk}, and Ag^0_{surf}) can be seen in **fig. S13**. The total amount of silver ions in solution for each light intensity over the course of the process follows a reversed S-shape curve indicating that the reduction of Ag^+ starts off slow. Then the rate of Ag^+ consumption rapidly increases until all Ag^+ ions are depleted (**fig. S13 A,C,E**), which results in a plateau. Ag^0, Ag^0_{bulk}, and Ag^0_{surf} also follow an S-shape curve over time for each light intensity (**fig. S13 B, D, F**). The surface atoms take up a greater fraction of the total atoms in the NPs at earlier synthesis times when the NPs are smaller. The percentage of total surface atoms in the NPs significantly decreases as the process continues due to slow increase in d.

Table S1. Rate constants k_1, k_2, and k_3 for varying light intensities.

Light Intensity	k_1 (min^{-1})	k_2 ([Ag^0_{surf}]$^{-1}$min^{-1})	k_3 ([NP]$^{-1}$min^{-1})
1.3 mW/cm^2	7.2x10^{-8}	8280	22800
8 mW/cm^2	2.93x10^{-7}	11800	28500
17.2 mW/cm^2	5.85x10^{-7}	21200	49400

The rate constants (Table S1) differ significantly from their biological counterparts, such as fungal and bacterial cells,[7,8] which is expected due to the different sizes of the particles (nanometer scale) and cells (micrometer scale).

Supplementary Text 11: Thermodynamics of resting size of NPs in chains

The average NPs in the chains and the quasi-steady-state size of NP_m in the system depend on the illumination conditions. It was found to be 13.6 ± 3.5 nm under electron beam, 6.6 nm ± 2.7 nm, 16.1 nm ± 2.2 nm, and 18.2 nm ± 2.1 after 30, 60, and 180 min of 365 nm illumination, respectively (**fig. S3**). These dimensions are determined by the thermodynamics of the NPs of different dimensions and the rate of the slow quasi-steady-state growth due to spontaneous capture of Ag^0 generated around each NP.

The fundamental reason for the restrictions on NP diameter for NP_m is the rapid drop in the chemical potential, μ, with the particle volume governed by the Gibbs−Thomson relation $\mu = 2\gamma V_m / r$, where r is the particle radius, V_m is the volume per atom, and γ is the surface energy (surface tension). The Gibbs−Thomson relation is applicable to NPs formed by any mechanism in solution. There is a substantial difference, however, with classical nucleation theory, non-classical crystallization mechanism, and electrochemical particle reduction.[5,9] Unlike the standard processes of NP nucleation, the limiting step of our reaction is the production of the photoejected electrons rather than nucleation. Then, the formation of Ag^0 is much slower than in chemical reduction because it requires absorption of a photon, ejection of electron, and its capture by Ag^+. Also important, the redox processes shown in **fig. S1A** occur in the vicinity of the previously formed particles because the silver atoms are produced because of the photoejection of electrons from metal NPs into the solvent. Special interfacial conditions facilitating the nucleation of new particles can also localize the space around NP_m where NP_d emerges,[10] which can also be observed in **Movie S3** and the screen shot sequence in **Fig 2B.**

Under these conditions, the photogenerated species of Ag^0 can attach to the formed NP_m or NP_d. There is also Ostwald ripening that takes place via transfer of Ag^0 from NP_d to NP_m when the latter have not reached the quasi-steady-state limit. Illumination also produces the critical nuclei that are substantially smaller than both NP_d and NP_m. It is estimated by Völkle, Gebauer, and Cölfen to be ca. 1.1-1.2 nm corresponding to a cluster of about 30-55 silver atoms,[6] which means that the chemical potential of Ag^0 in the critical nuclei is substantially higher than that of NP_d and NP_m. When both NP_d and NP_m are present, critical nuclei are rapidly consumed via Ag^0 transfer to both, which can be observed in the snapshot sequence shown in **Fig.2**.

NP_m in this system represents, therefore, the thermodynamic sink in this system, which tends to consume both critical nuclei and NP_d. The mother-daughter competition for Ag^0 will determine the resting size of NP_m according to the chemical equation:

$$NP_m \leftrightarrow Ag^0 \leftrightarrow NP_d \qquad \text{(Eq. S14)}$$

The difference in chemical potential between NP_d and NP_m, with some contribution from the surface conditions, will determine the resting size of NP_m when it stops growing. The diameter of NP_d is ~ 5 nm based on information shown in **Fig 1**, **Fig. 2**, and **Movie S3.** They are smaller than the NPs in the chains but larger than the ones in the critical clusters of classical nucleation theory. Nevertheless, the chemical potential of Ag^0 atoms in NP_d is higher than that of NPs with a resting size.

In the first approximation, the free energy of the transfer of Ag^0 from NP_d to NP_m, ΔG_{NP}, will be the difference between the energy increase due to expansion of the particle-water interface of NP_m and energy decrease due to the transfer of silver atoms between the particles:

$$\Delta G_{NP} = 4\pi r^2\gamma - (4/3)\pi r^3 \rho_s \Delta\mu \qquad \text{(Eq. S15)}$$

where γ denotes the surface energy of the Ag/water interface, ρ_s is the density of Ag = 10,500 kg/m^3, and $\Delta\mu$ is the difference in chemical potential of Ag^0 between 'mother' particle in the slow quasi steady state growth stage and rapidly growing 'daughter' particles. To determine the particle radius when the growth stops, we assume $\Delta G_{NP} = 0$ and rewrite Eq. S15 as:

$$4\pi r^2\gamma = (4/3)\pi r^3\rho_s\Delta\mu \quad \text{(Eq. S16)}$$

$$r = 3\gamma / \rho_s\Delta\mu \quad \text{(Eq. S17)}$$

Bastian calculated that γ = 1.05 J/m^2,[11]. The value of $\Delta\mu$ for NP_m and NP_d can be estimated based on the chemical potential dependence on particle size. This was established by Rumptz, Mao, and Campbell[12] as $\Delta\mu$ ~10 kJ/mol, which is similar to what can be estimated based on the formula for adsorbed particles from Plesoff and Campbell[13] as:

$r = 3\cdot 1.05$ J/m^2 / (10500 kg/m^3 · 1000g/kg / 107g/mol ·10000 J/mol) = $3.2\cdot10^{-9}$ m = 3.2 nm, which gives the diameter of ***d* = 6.4 nm**.

When comparing this theoretical estimate with the experimental data of NP_m diameters, we note that NP_m particles in the middle of the chains underwent slow growth under electron beam, which resulted in *d* = 13.6+/-3.5 nm, obtained for NP self-replicated under electron beam illumination as well as for the NP chains with *d* = 16.1 nm ± 2.2 nm after 60 min of illumination (**fig. S3**) and *d* = 18.2 nm ± 2.1 nm after 180 min of illumination. The calculated value of *d* = 6.4 nm matches well with the average diameter of NPs after 30 min of illumination under self-replicating conditions, *d* = 6.6 nm ± 2.7 nm (**Fig. 1C, fig. S3**). It is also very close to the NP size of ~8-9 nm identified in cryo-TEM data shown in **Fig.1E** for the actual NP_m at 60 min.

Supplementary Text 12: Electroless deposition

The substrates with and without NP networks were exposed to the standard electroless deposition solution for five minutes. The silver is deposited only on NP networks catalysed by the metallic surface. As expected, the overall rate of the deposition is dependent on the NP surface density (**fig. s19)**. When soaked for a prolonged period (up to 40 min), all the growth islands become connected and create a thin film of silver atoms across the surface of the substrate.

A control was performed by trying to deposit silver on a glass slide functionalized by $(PDDA/PSS)_3PDDA$ multilayers but without any NPs; no silver deposition was observed.

Supplementary Text 13: Calculations of fractal dimensions

ImageJ software is used to analyze the fractal characteristics of the SEM images. A binary version of each processed image is generated, a prerequisite for the application of the *FraLac* plugin application, which facilitates the fractal analysis procedures. Using the *FraLac* plugin, the parameters for box counting analysis were configured and executed to yield results pertaining to the fractal characteristics, specifically, the fractal dimension of the examined images (**fig. S21**).

Supplementary Text 14: Graph Theoretical (GT) analysis of NP, bacterial, and fungal networks

The GT parameters were extracted using the open source *StructuralGT* software. Both literature and original data can be evaluated using this Python code with dedicated GT and interface modules.[14]

Supplementary Text 15 Electromagnetic Simulations.

The analysis of the electromagnetic field for Ag NPs was conducted using the *Lumerical* FDTD Solutions commercial software package, 2020 R2. Models for this analysis were generated through Autodesk 3ds Max software, guided by TEM observations. The electrical and magnetic fields were assessed by frequency profile monitors, with light excitation at 365 nm along the *z*-axis. The light absorption and scattering spectra were obtained through two distinct analysis groups, each focusing on a specific experimental wavelength region. The refractive indices applied to Ag, ZnO, and Fe_3O_4 were sourced from established databases and a refractive index of 1.33 was simulated for a water environment.

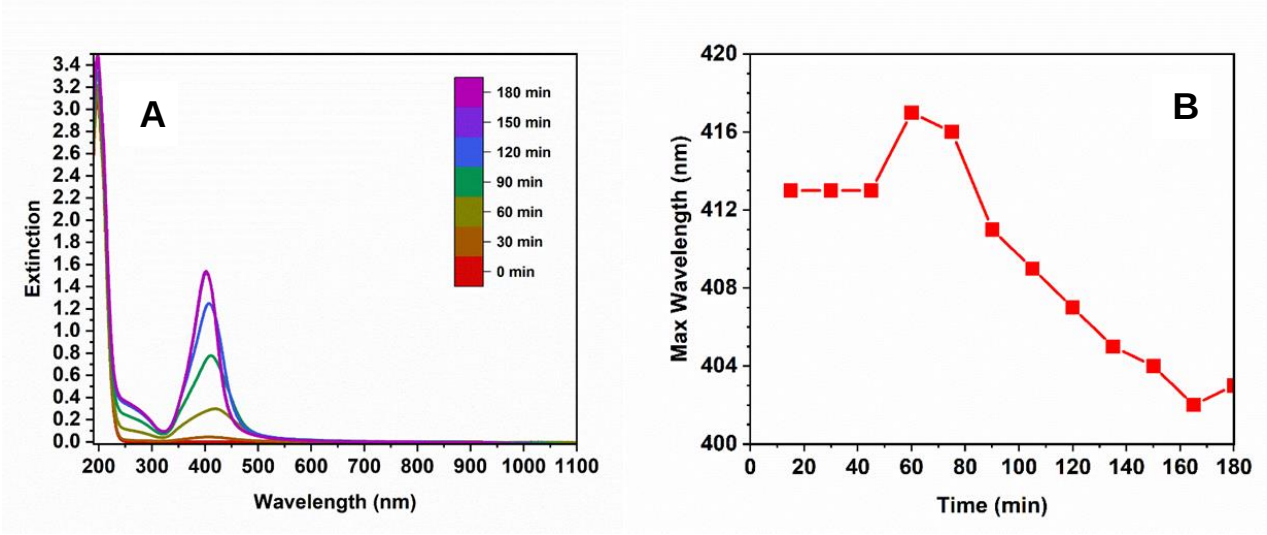


Fig. S1. Photochemistry of the light-driven autoicatalytic self-replication and self-assembly of NPs into chains and networks. (**A**) Extinction spectra obtained from UV-Vis spectroscopy for every 30 min during the photoinduced autocatalytic self-replication and self-assembly process of NPs in (A). (**B**) Temporal dependence of the peak wavelength in the extinction spectra.

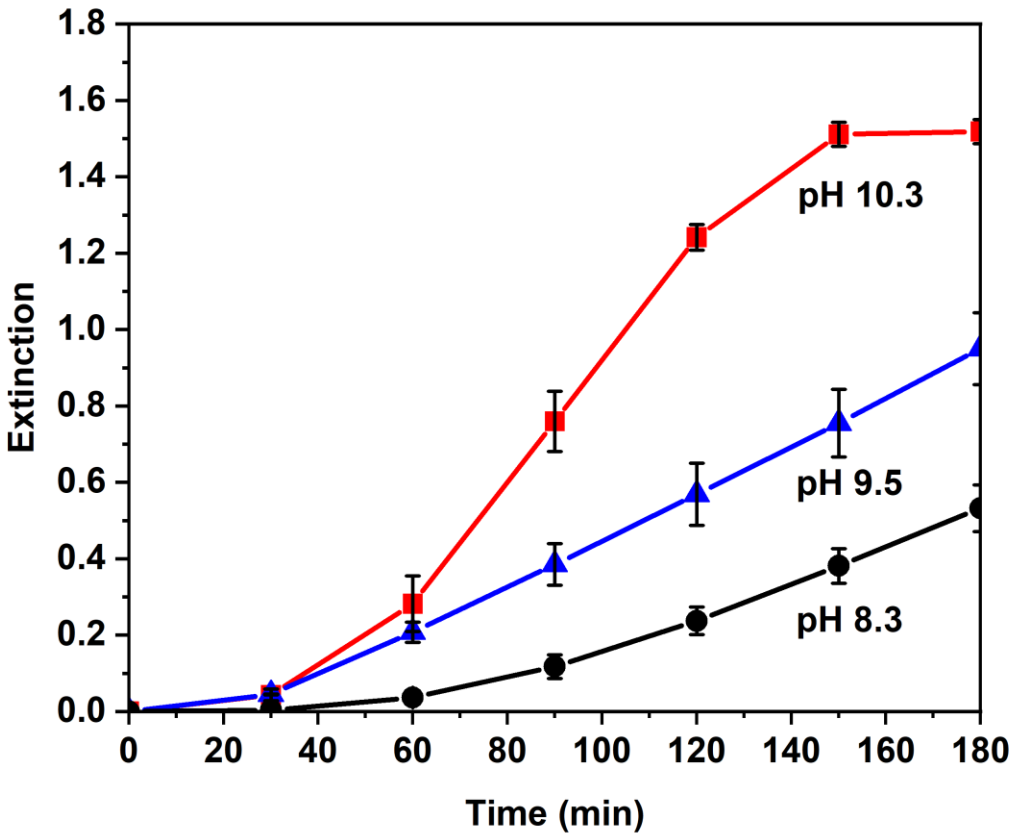


Fig. S2: Kinetic curves for NP accumulation at different pH values of silver nitrate/sodium citrate dihydrate solution illuminated at 365 nm UV light. The maximal extinction intensity from the UV-Vis spectra for pH 8.3 (black), 9.5 (blue), and 10.3 (red). Each dispersion was analysed at 30 min time intervals up to 180 min.

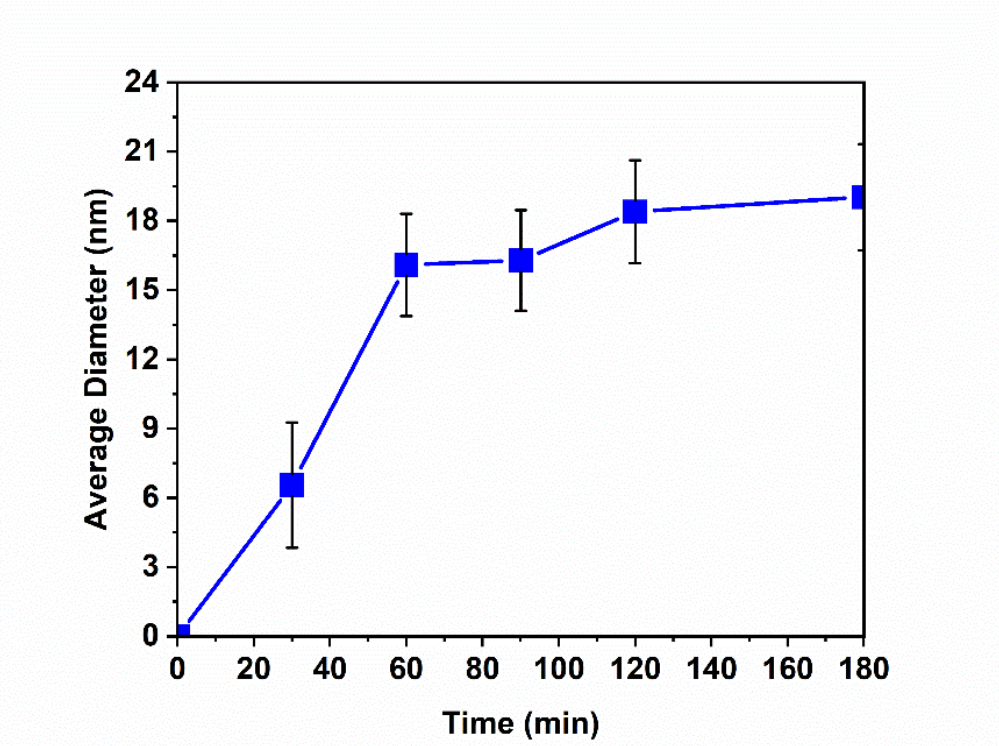


Fig. S3: Plot of average diameter, *d*, for NPs in the course of light-driven autocatalytic self-replication and self-assembly. Average diameters were measured for more than 100 NPs at each time point. The slow growth of the NPs is related to the finite probability of plasmon localization on any NP in the chain and the gradual accumulation of citrate oxidation products leading to destabilization of the NPs.

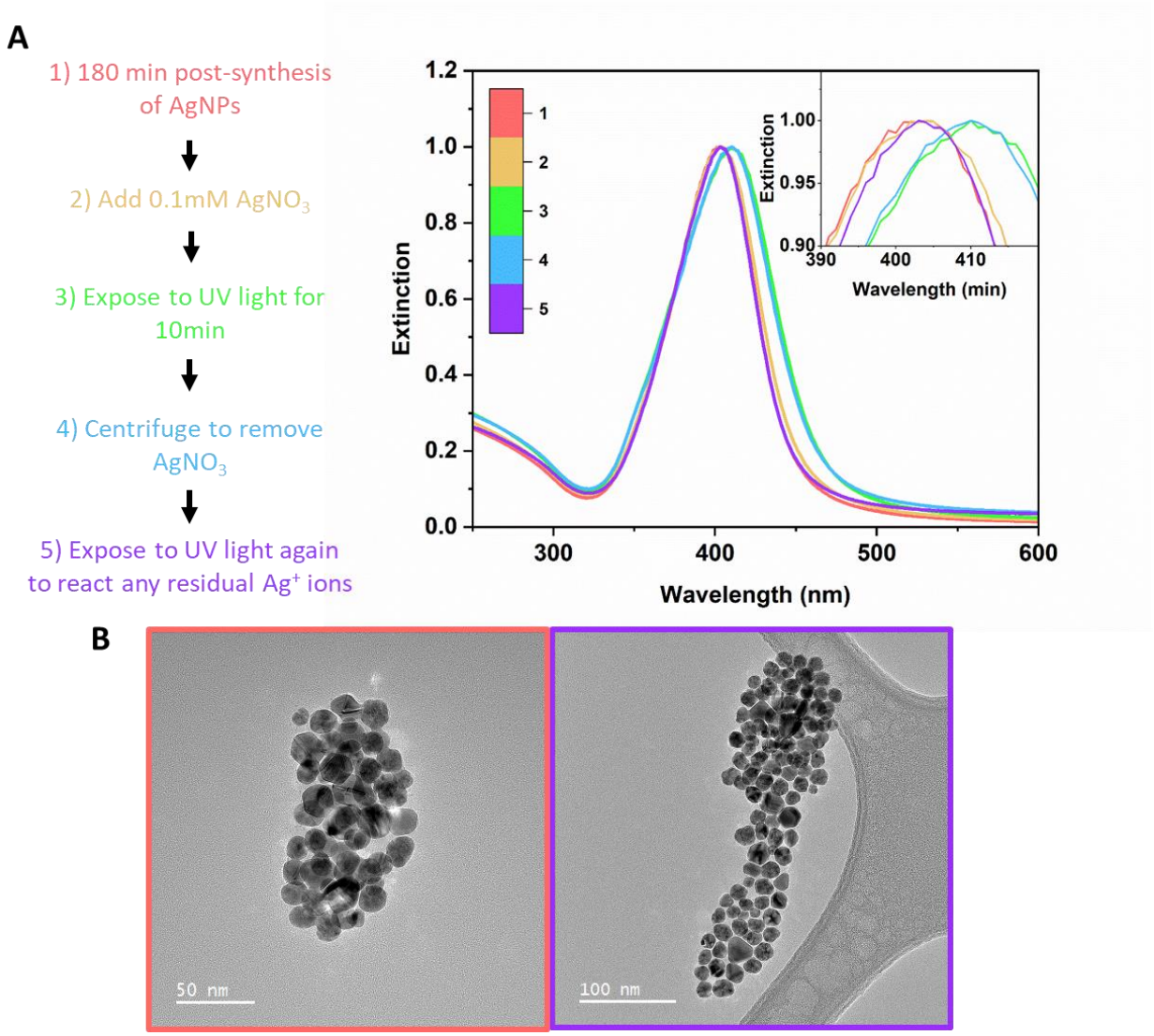


Fig. S4. Blue-shift in extinction peak over time. (**A**) Shift in max wavelength of extinction due to electron density of NPs changing during the synthesis. All extinction spectra are normalized to 1 to show a clearer comparision of the wavelength shift. (**B**) TEM images of NPs at the start (1) and end (5) of the post-synthesis analysis. Border color matches between each TEM image and the extinction spectrum.

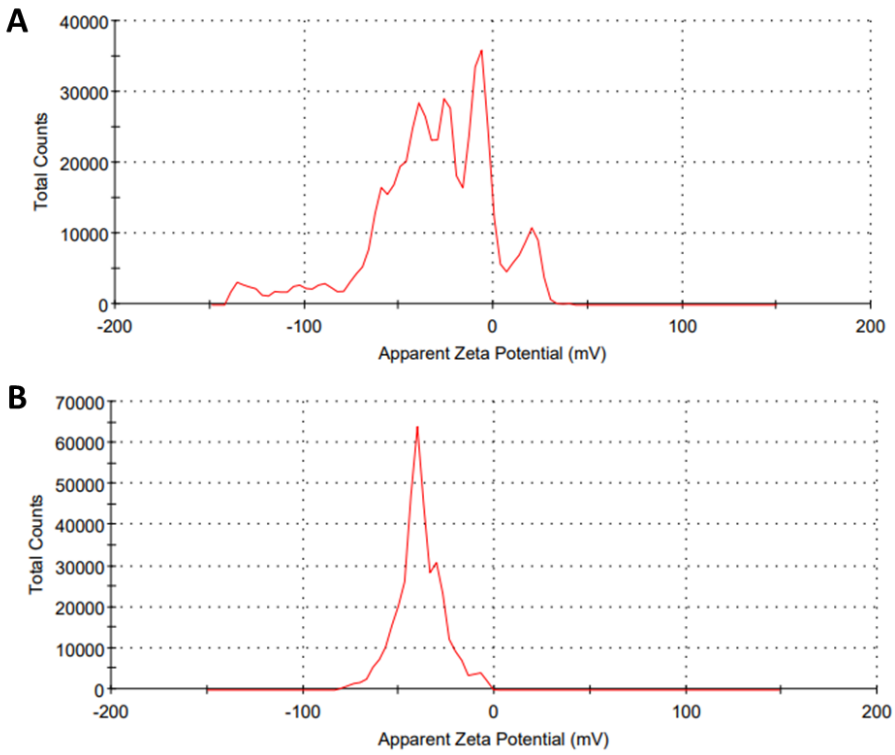


Fig. S5. Zeta-potential of silver NPs and their chain assemblies. (**A**) Post-reaction zeta-potential (mV) of self-replicating NPs. (**B**) Zeta-potential disctribution of commercial monodisperse 20 nm NPs (Sigma-Aldrich).

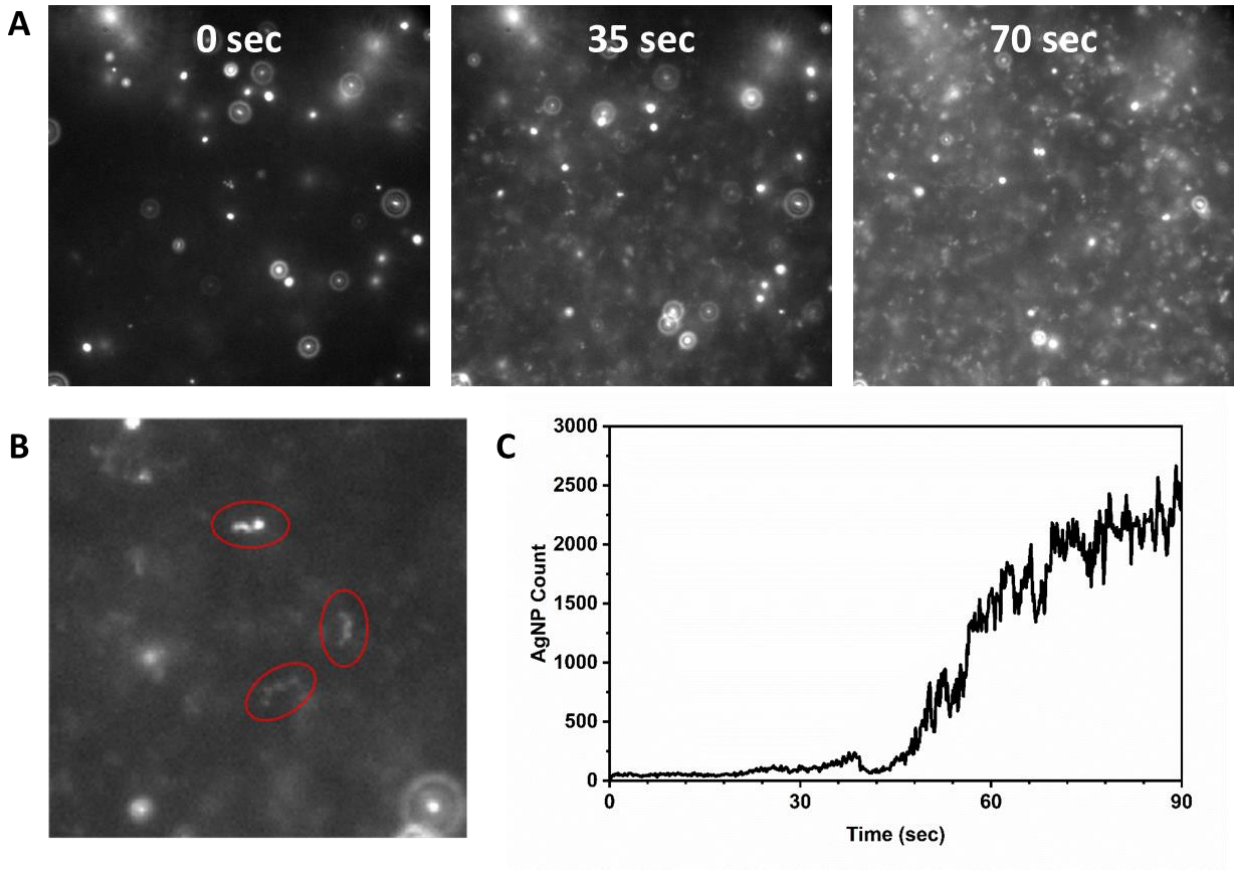


Fig. S6. Dark-field microscopy of NPs in the course of photoinduced autocatalitic self-replication and self-assembly. (**A**) Dark field microscopy stillshots at 25 second intervals. (**B**) tracking the number of NPs/chain assemblies (circled in red). (**C**) Formation of NP chains over time.

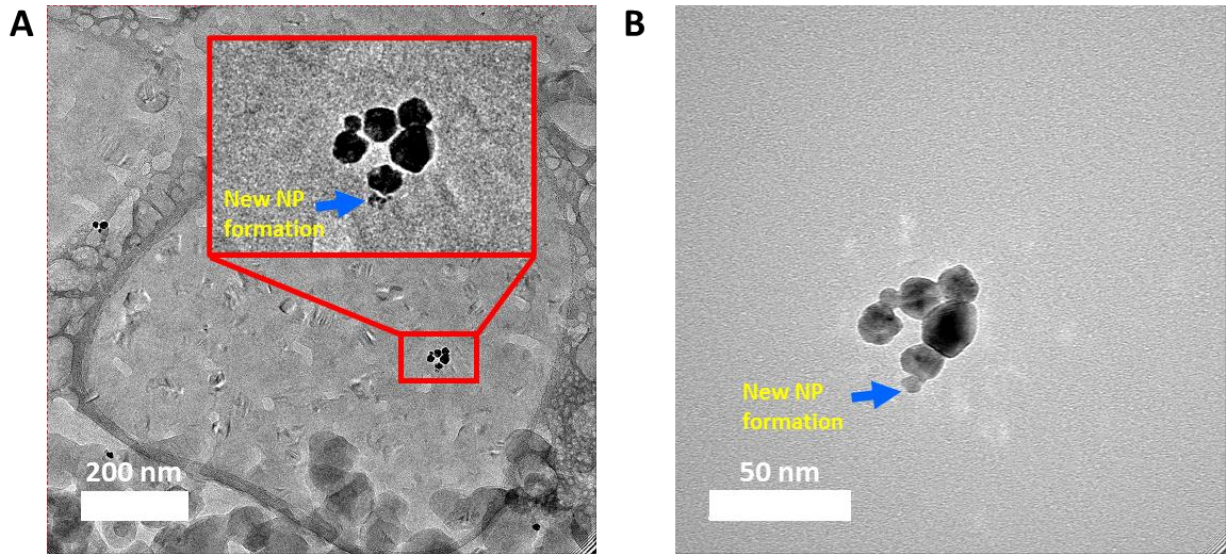


Fig. S7. Nucleation of a NP_d next to a NP_m. (**A**) Cryo TEM image of NP clusters aggregating at the end of the NP chain. (**B**) Cryo TEM image of NP_d formation after allowing the electron beam to melt the ice.

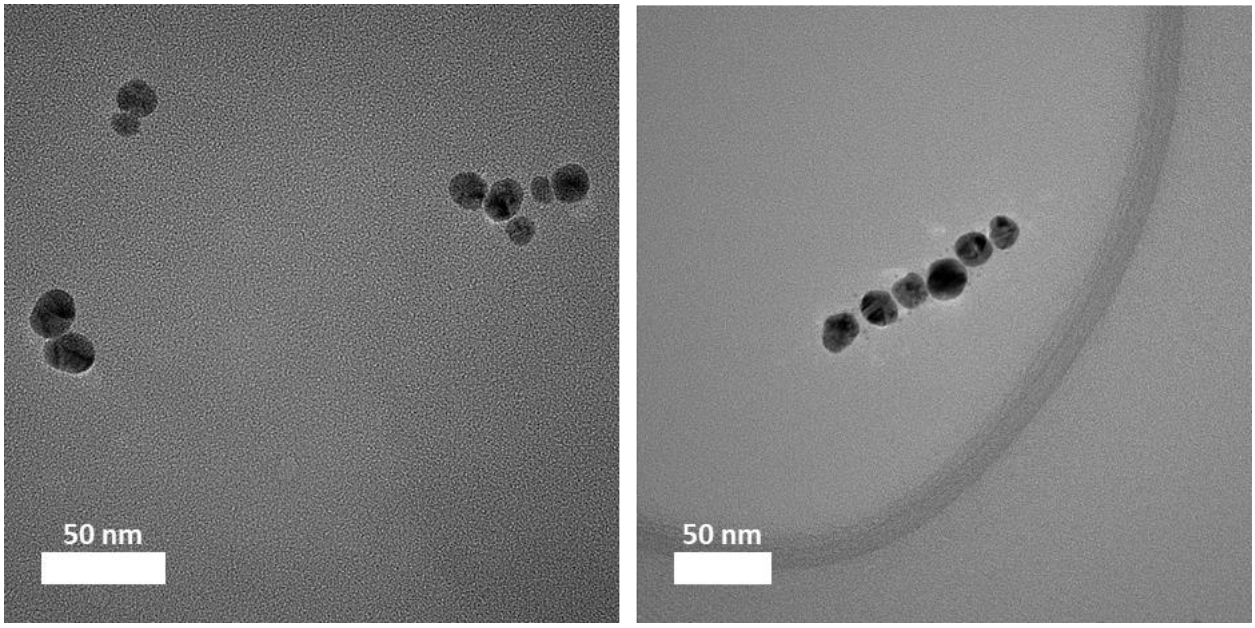


Fig. S8. TEM images of self-assembly of NP chains in the early stages of the network formation. The multilayers with the architechture of of $(PDDA/PSS)_3$ PDDA with the final positively charged layer were deposited directly on the TEM grid following the standard LBL processing protocol from 1% solutions of the polyelectrolytes.

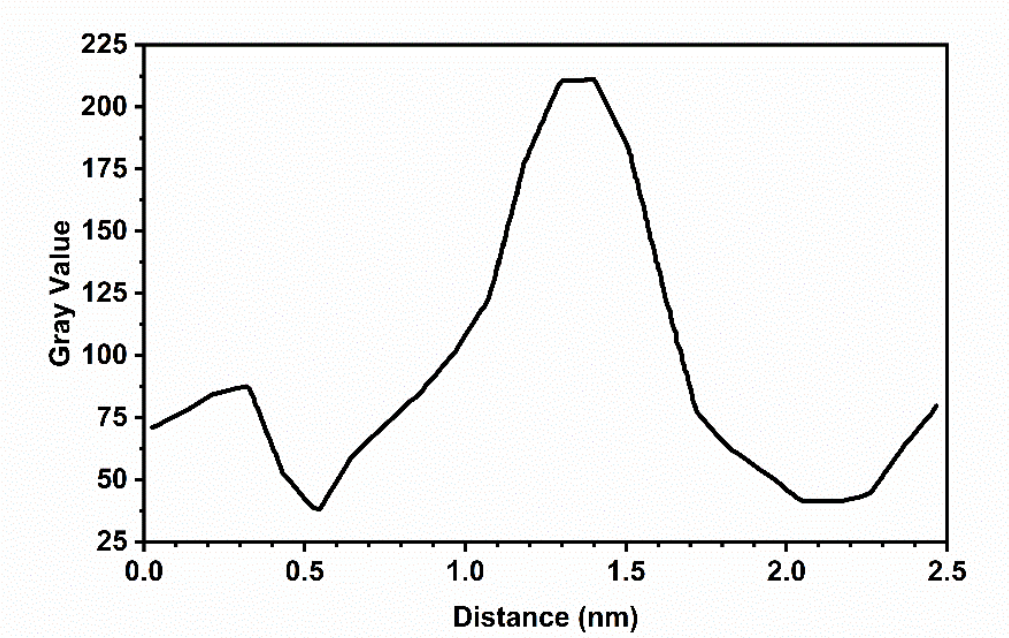


Fig. S9: Characteristic distance for self-replication of NPs. The variation of the gray value over the distance between two NPs in the chain assemblies in **Fig. 1E**.

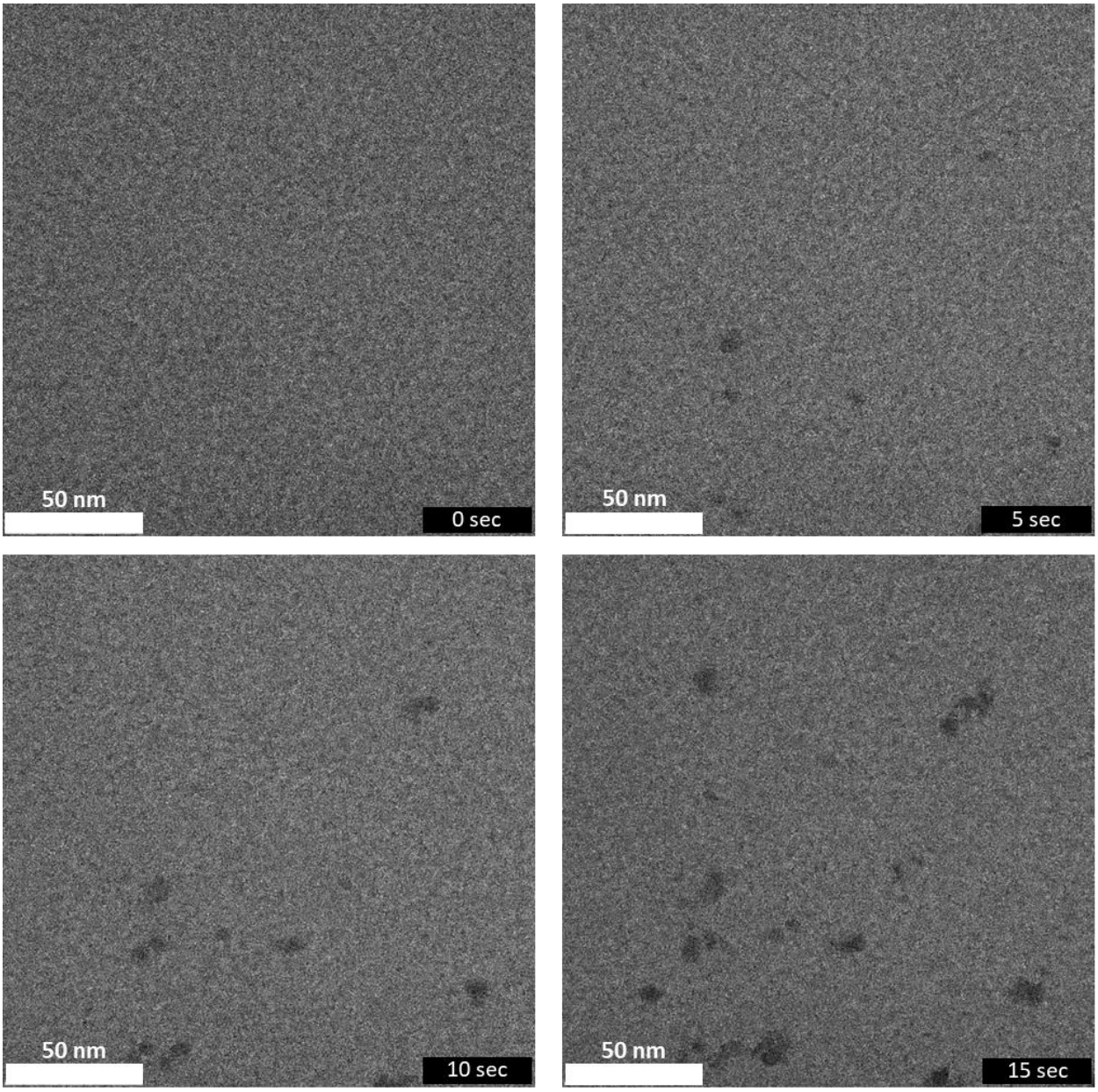


Fig. S10. LPTEM images for the NP system at pH 8.3 as a control experiment for conditions when S-curve NP accumulation kinetics was not observed. The rate of the generation of Ag^0 and post-synthetic growth of NPs in quasi-steady state conditions is drastically reduced because no NaOH was added. NP nucleation under electron beam takes place but their formation is weakly autocatalitic under these conditions. The tendency to self-assemble is also diminished but not completely impeded.

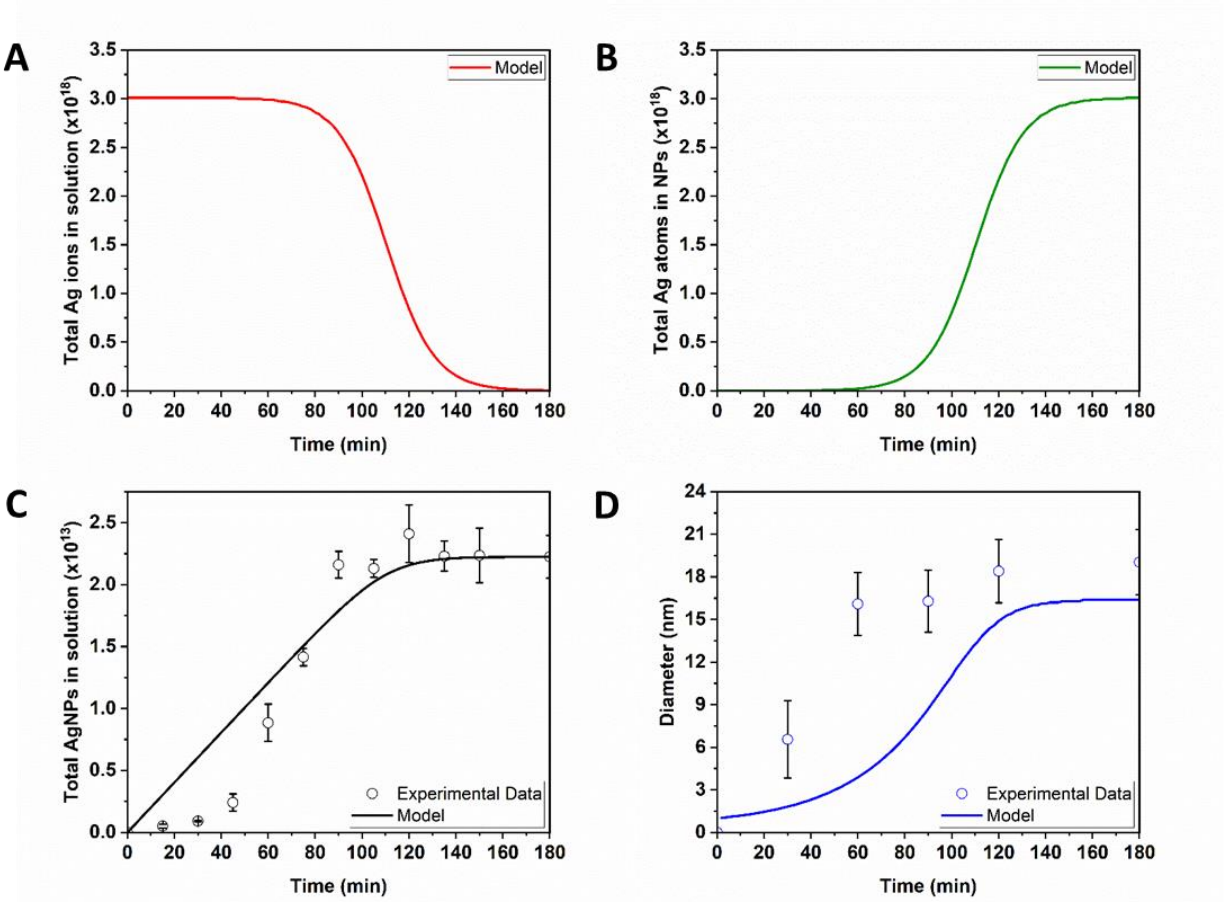


Fig. S11: Fitting experimental data to the Finke-Watzky (FW) model. (**A**) Theoretical concentration of Ag^+ ions in solution over the course of the synthesis from the Finke-Watzky model. (**B**) Theoretical total number of Ag^0 atoms in all NPs over the course of the synthesis from the Finke-Watzky model. (**C**) Fit of the Finke-Watzky model (line) to the experimental NP concentration (hollow circles) over time. (**D**) Fit of the Finke-Watzky model (line) to the experimental average NP diameter (hollow circles) over time.

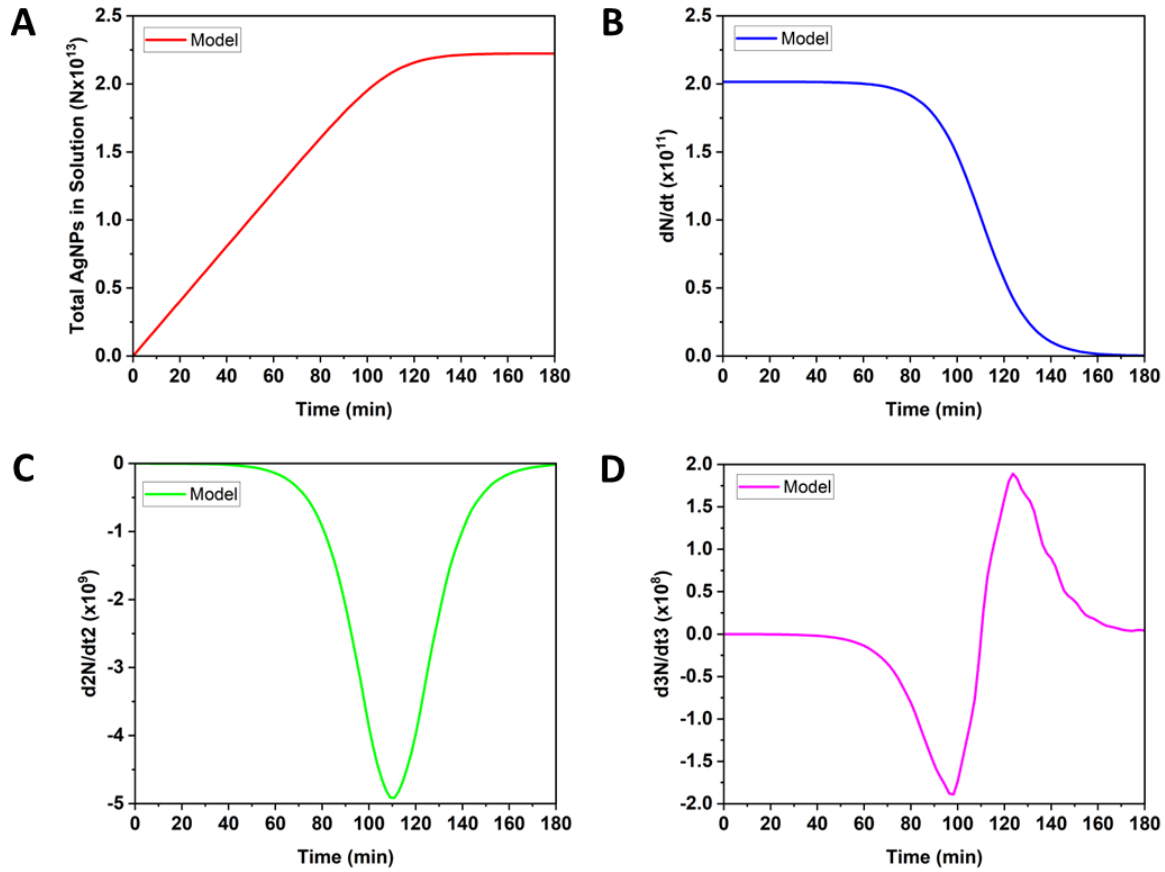


Fig. S12: Derivatives of Finke-Watzky model fitted to experimental data. (**A**) Fit of the Finke-Watzky model to experimental NP concentration from fig. S11C**.** Temporal dependences for (**B**) *rate of NP formation* (*dN/dt*); (**C**) *acceleration* (d^2N/dt^2); and (**D**) *jerk* (d^3N/dt^3).

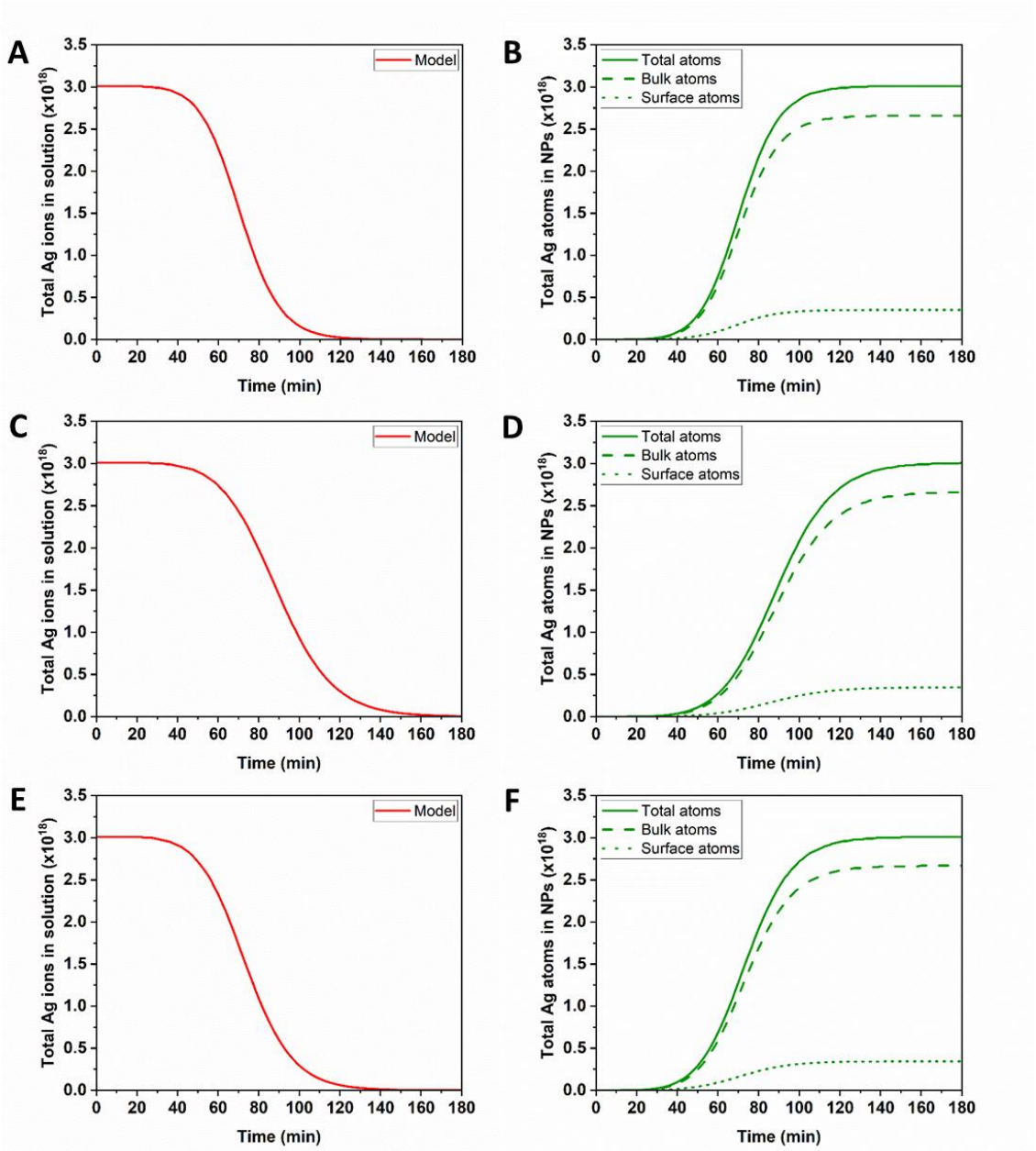


Fig. S13. Theoretical silver ion/atom changes over time from self-replication kinetic model. (**A,B**) Model calculations for synthesis at 1.3 mW/cm^2 light intensity for (A) total unreacted silver ions in solution and (B) total reacted silver atoms in all NPs (solid line) along with atoms encompassing the bulk (dashed line) and surface (dotted line) of the NPs. (**C,D**) Model calculations for synthesis at 8 mW/cm^2 light intensity for (C) total unreacted silver ions in solution and (D) total reacted silver atoms in all NPs (solid line) along with atoms encompassing the bulk (dashed line) and surface (dotted line) of the NPs. (**E,F**) Model calculations for synthesis at 17.2 mW/cm^2 light intensity for (E) total unreacted silver ions in solution and (F) total reacted silver atoms in all NPs (solid line) along with atoms encompassing the bulk (dashed line) and surface (dotted line) of the NPs.

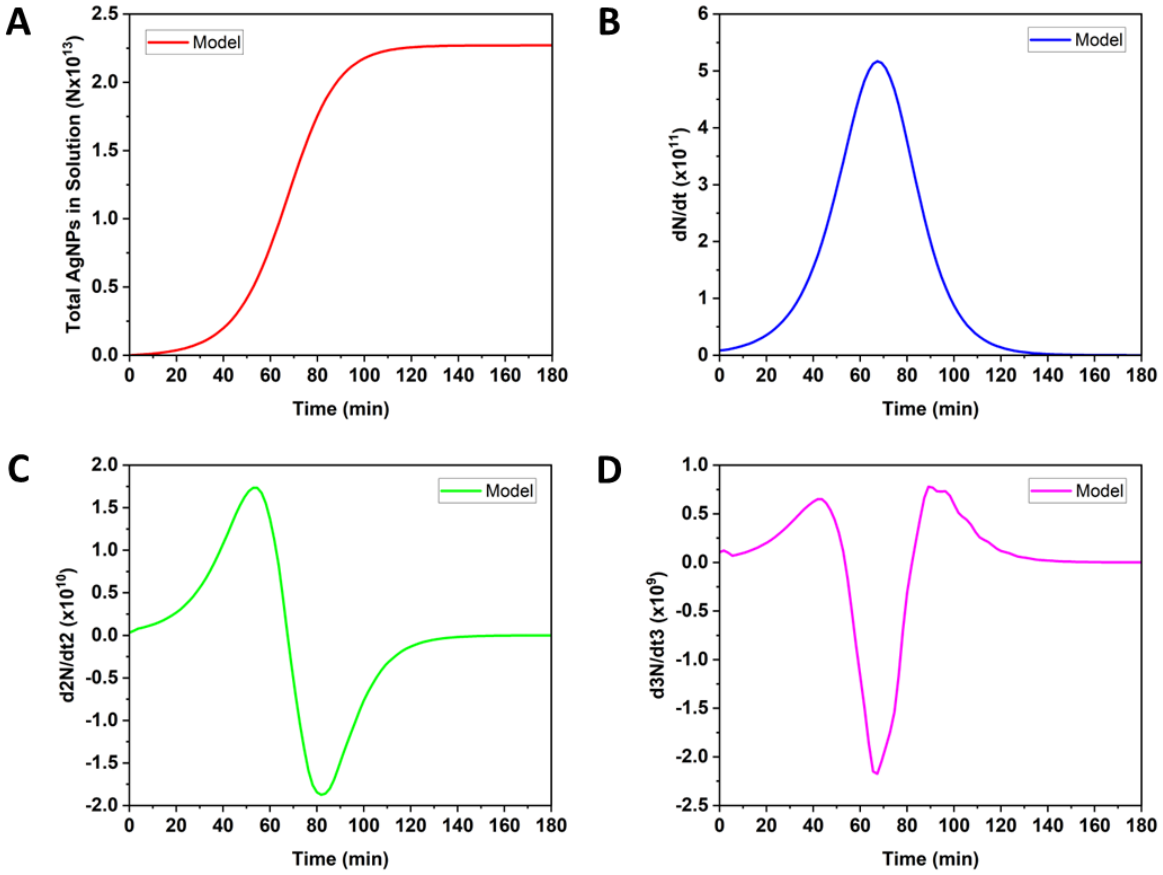


Fig. S14: Derivatives of self-replication kinetic model fitted to experimental data. (**A**) Fit of the self-replication kinetic model to experimental NP concentration from **fig. 3A**. Temporal dependences for (**B**) *rate of formation (d[NP]/dt)*; ***(C)*** *acceleration* ($d^2[NP]/dt^2$); ***(D)*** *jerk* ($d^3[NP]/dt^3$) of NPs.

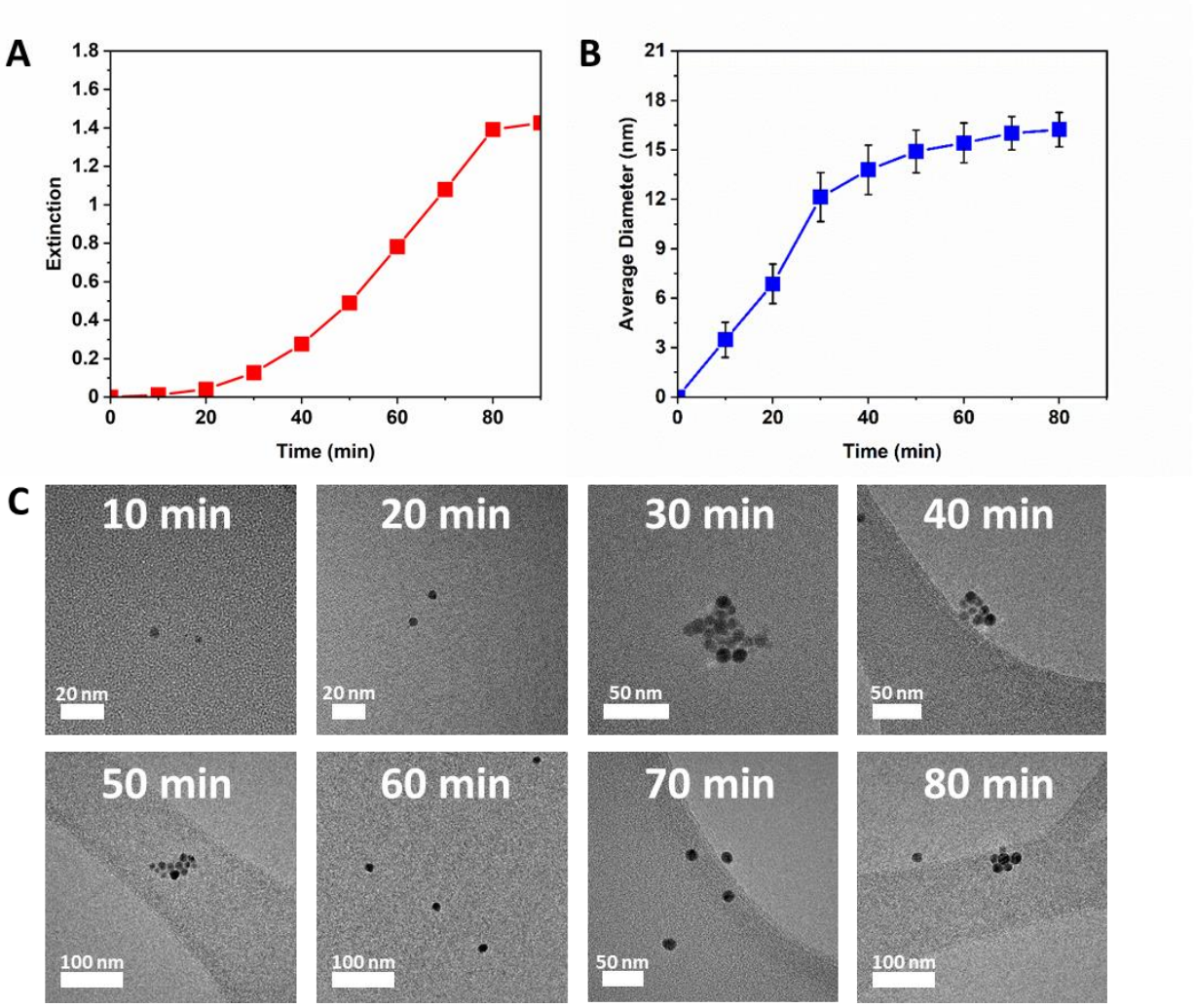


Fig. S15. Self-replication of NPs for 8 mW/cm^2 light intensity illumination. (**A**) The amplitude of the light extinction maximum at different time points during the illumination. (**B**) Average diameter at different time points during the illumination. (**C**) Exemplary TEM images of NPs for different time points during the illumination.

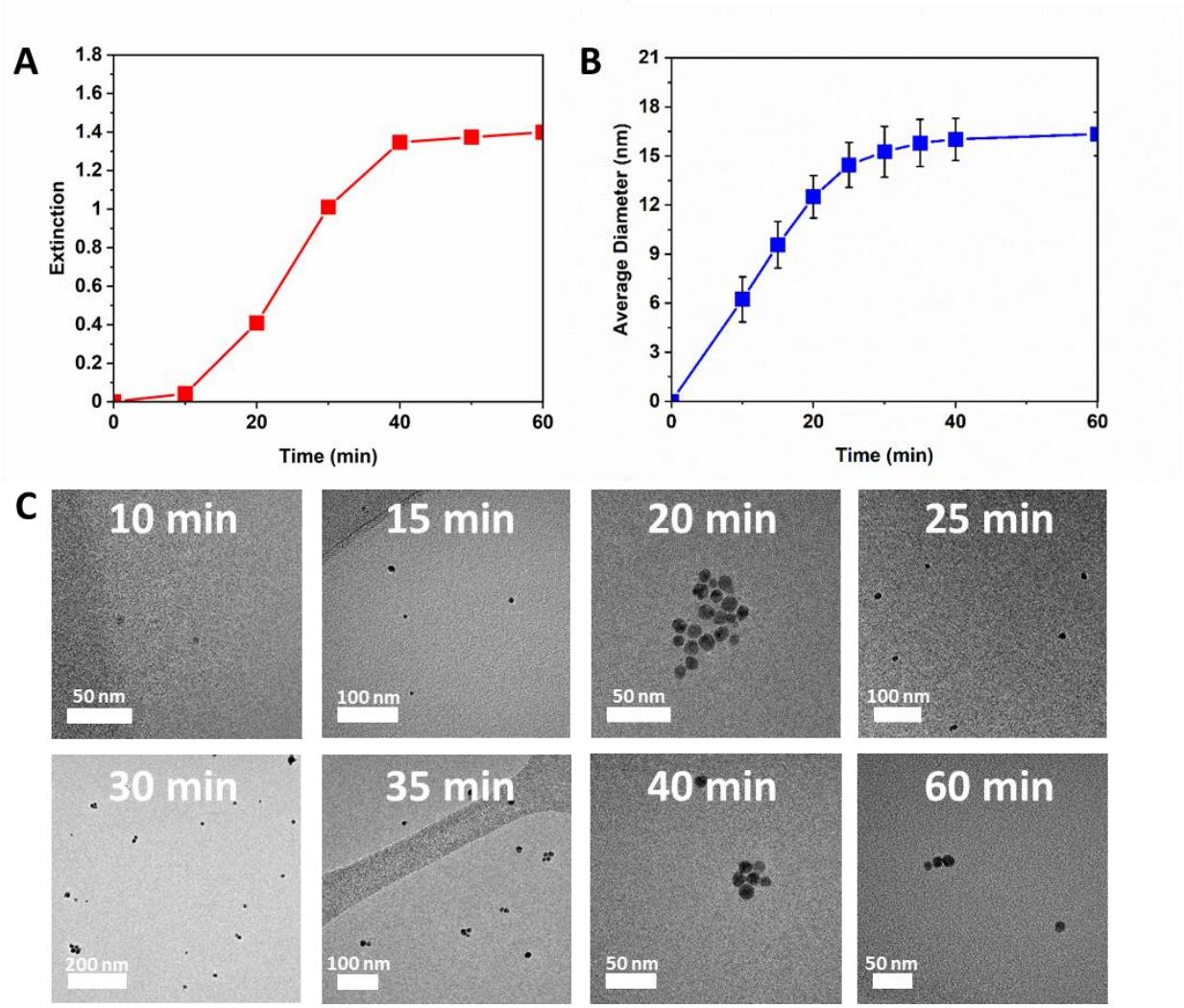


Fig. S16. Self-replication of NPs for 17.2 mW/cm^2 light intensity illumination. (**A**) The amplitude of the light extinction maximum at different time points during the illumination. (**B**) Average diameter at different time points during the illumination. (**C**) TEM images of NPs at different time points during the illumination.

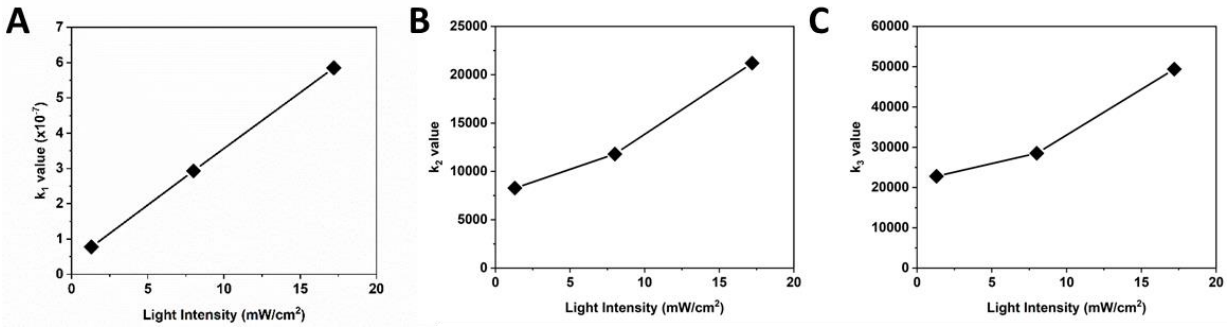


Fig. S17. Dependence of the self-replicating rate constants on light intensity. (**A**) Rate constant k_1, (**B**) rate constant k_2, and (**C**) rate constant k_3, according to the experimental fit of system from Eq. S4, S5, and S6 (Table S1).

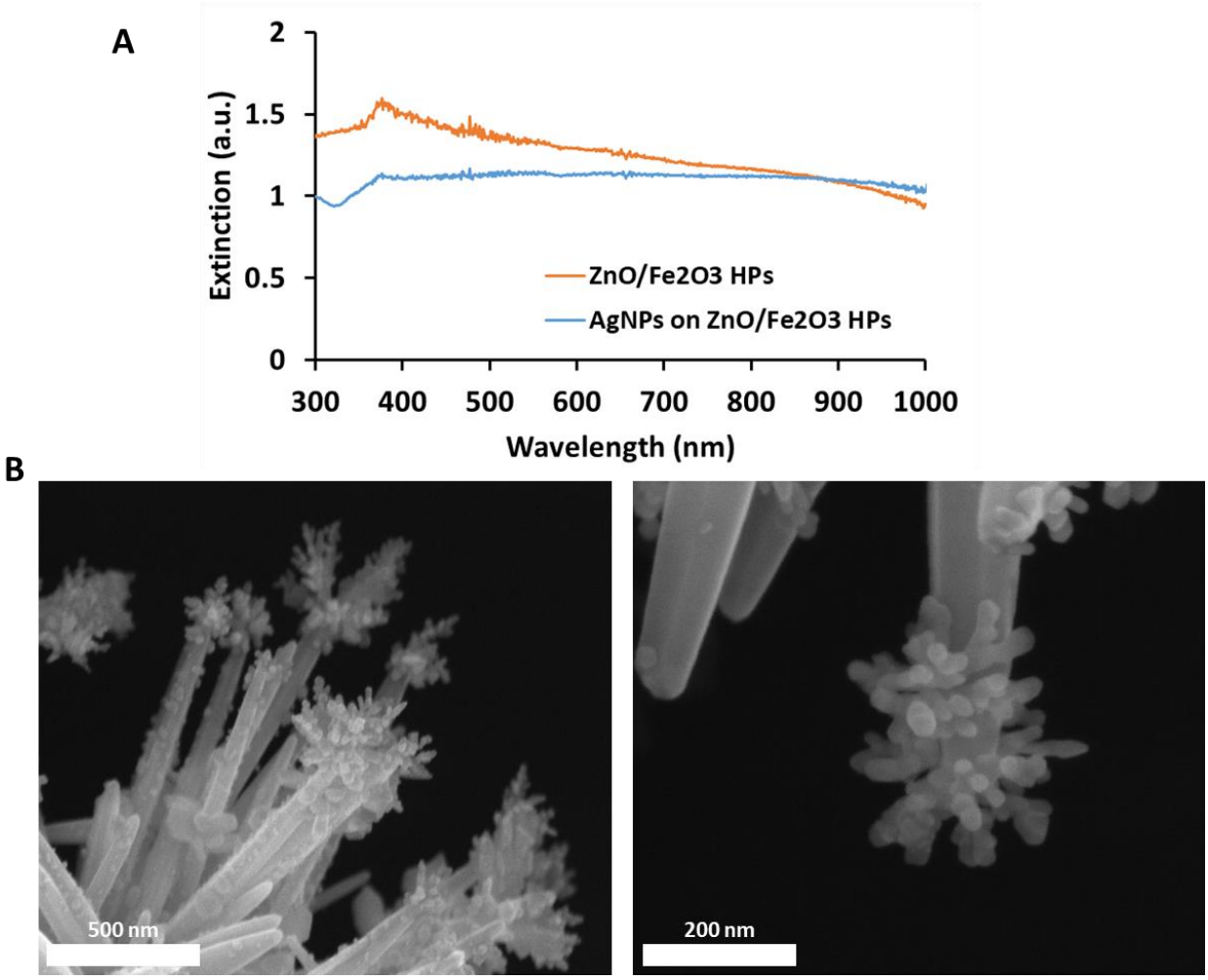


Figure S18: Self-replicating NP networks grown on spiky ZnO/Fe_2O_3 hedgehog particles (HPs). (**A**) Extinction spectra of bare ZnO/Fe_2O_3 HPs and those carrying interconnected network of self-replicating NPs grown on the tips of spikes on ZnO/Fe_2O_3 HPs. (**B**) SEM images of interconnected network of self-replicating NPs grown on the tips of spikes on ZnO/Fe_2O_3 HPs. The localization of the growth sites on the apexes of the spikes is guided by the electromagnetic singularities.

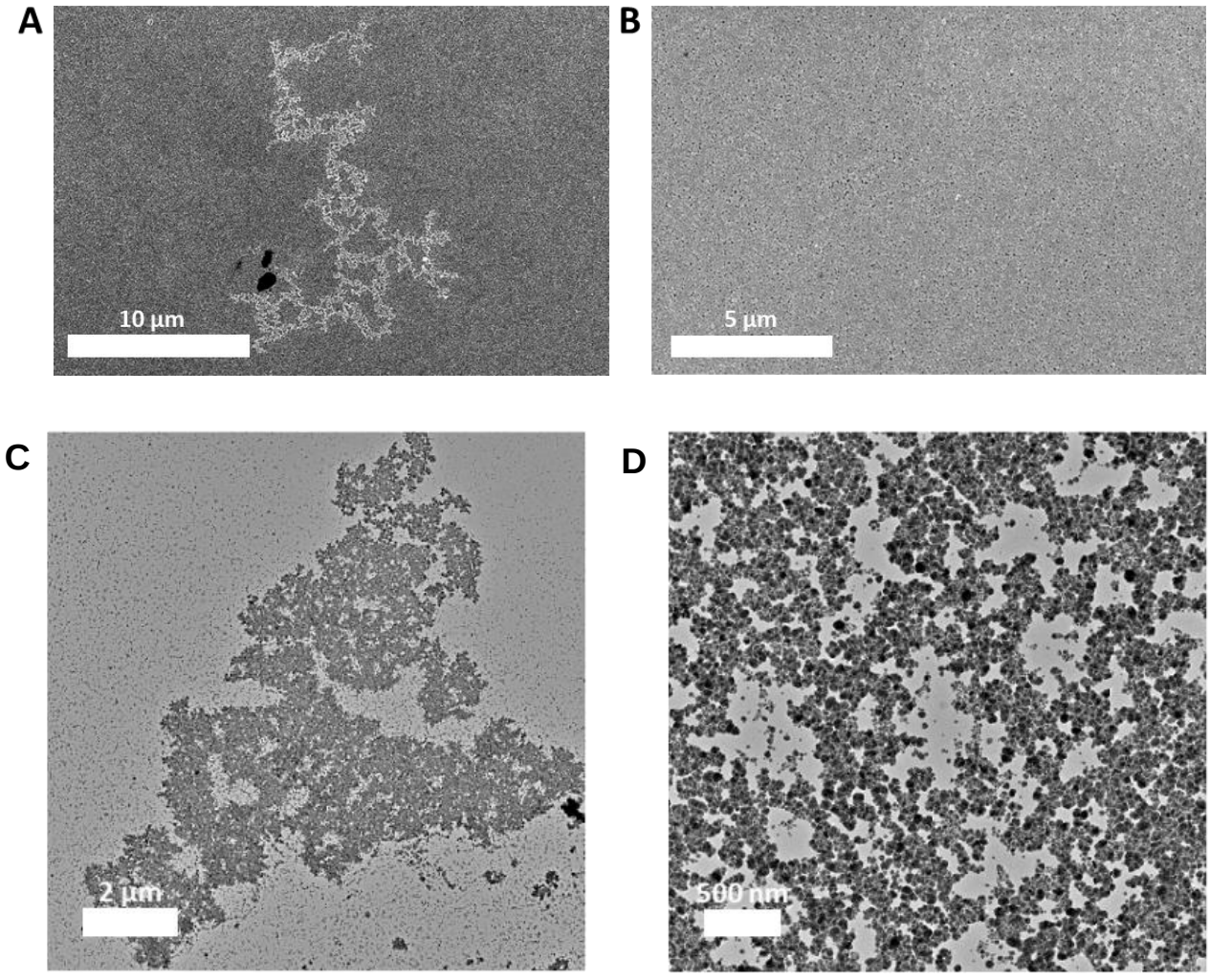


Fig. S19: Electroless silver deposition over the self-replicating NP networks. (**A**) SEM image of a 40 min electroless silver deposition on the NP networks supported on a glass slide functionalised by $(PDDA/PSS)_3PDDA$ multilayers. (**B**) SEM image of the growth of the 40 min electroless silver deposition ~50-100 µm away from the NP network. (**C,D**) TEM images of a 5 min electroless silver deposition onto the NP networks formed on the TEM grid functionalized with LBL multilayers in different magnification.

The obtained sheet resistance can be as low as **60 ohm/sq,** which is comparable or better than those of many conductive films used in biosensing, optoelectronics, and wearable devices.

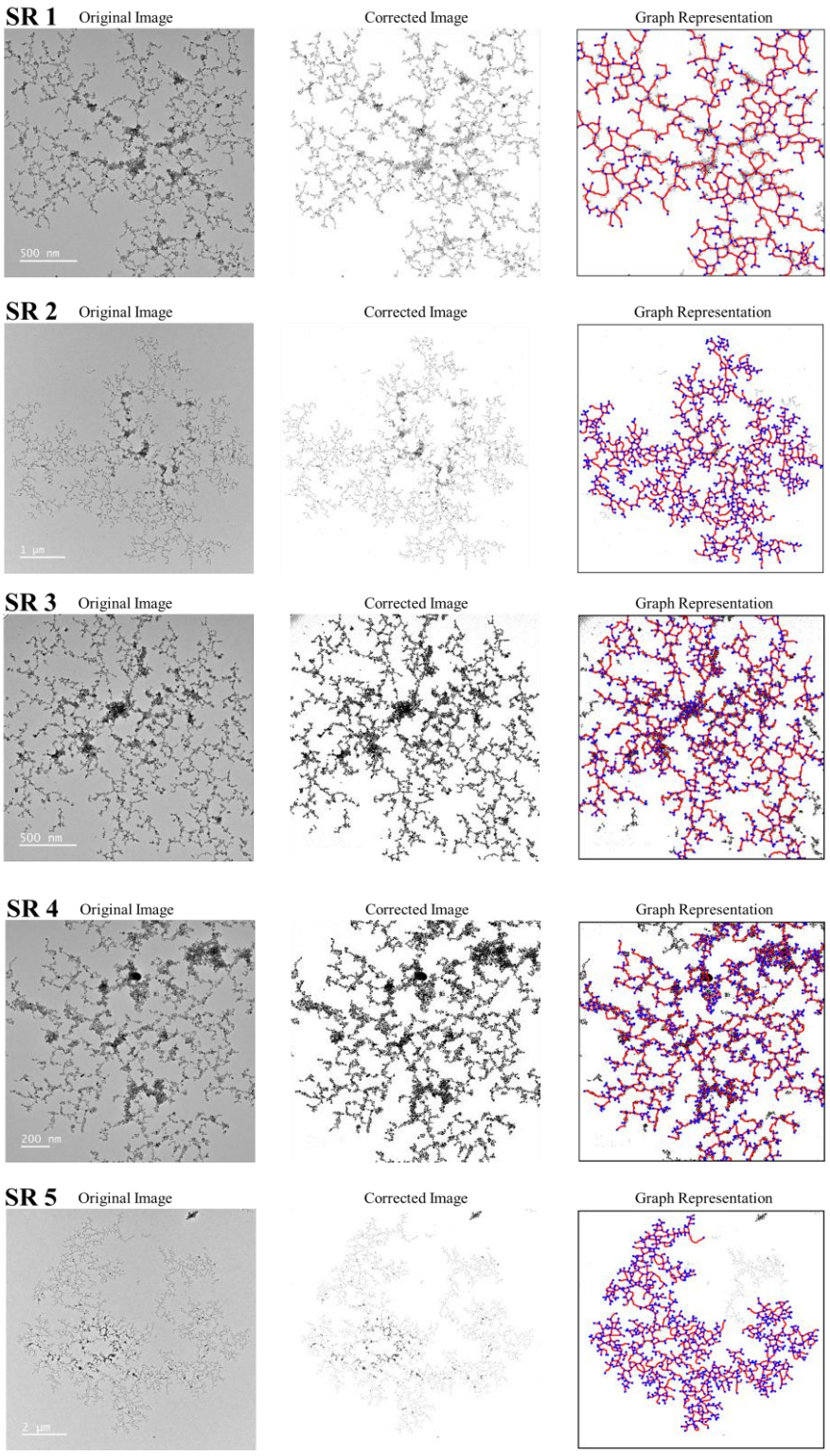


Fig. S20. Networks of self-replicating NPs and their GT representations. The NP networks grown by illumination of TEM grids placed on the surface of standard growth solution (see Methods). The grids were coated with $(PDD/PSS)_3PDDA$ multilayer sequence following the standard protocol from 1% aqueous solutions prior to formation of NP networks.

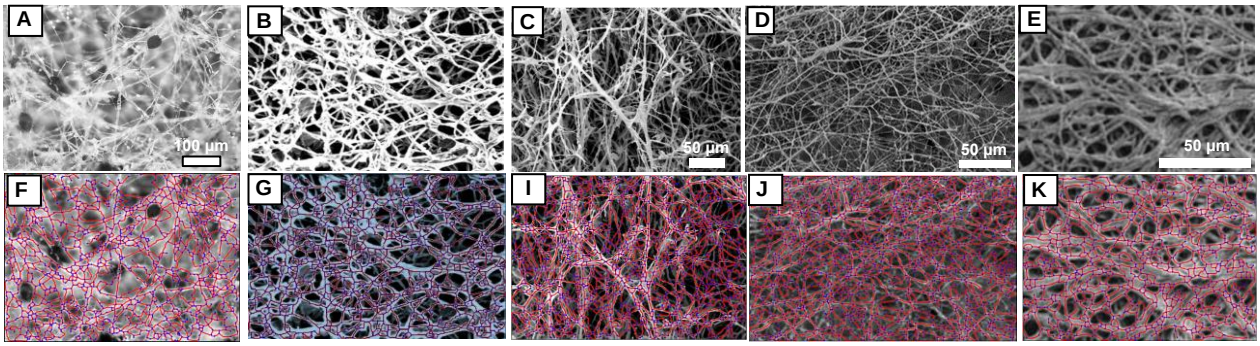
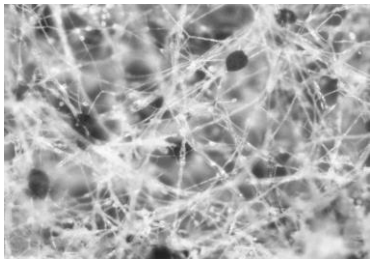
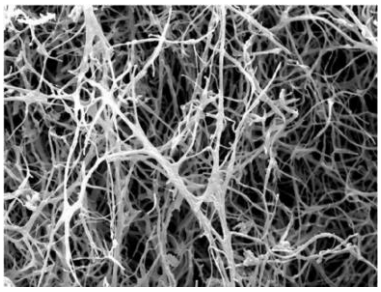
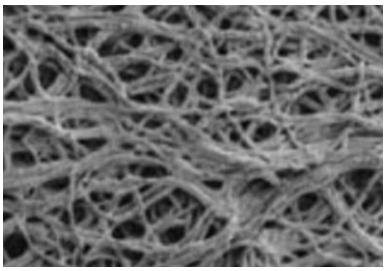
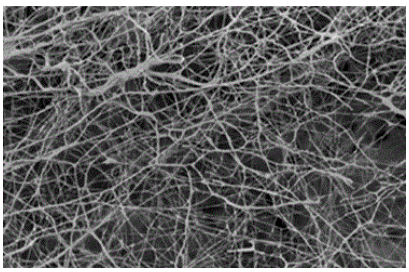


Fig. S21. Microscopy images of fungal networks (A-E) and their graphs (F-K). (**A, F**) *R. stolonifera* biofilm grown on *Capsicum annuum L*. (**B, G**) *Aspergillus fumigates* biofilm grown on confluent layer of human bronchial epithelia cells[15]. The original image does not have scale bar; GT representation does not depend on the physical scale. **(C, I)** *Trametes versicolor* biofilm grown on wheat grains[16]. **(D, J)** *Ganoderma lucidum biofilm* grown on wood[17]. (**E, K**) *Aspergilus Niger* 55890 biofilm grown on agar[18].

R. stolonifera biofilm grown on *Capsicum annuum L* (our data)	
	Average Degree 2.83 Clustering Coefficient 0.075 Average Nodal Connectivity 2.34 Assortativity Coefficient 0.076 Fractal Dimension 1.879
Trametes versicolor biofilm grown on wheat grains[11].	
	Average Degree 2.905 Clustering Coefficient 0.071 Average Nodal Connectivity 2.502 Assortativity Coefficient 0.0108 Fractal Dimension 1.879
Aspergilus Niger 55890 biofilm grown on agar[8].	
	Average Degree 2.846 Clustering Coefficient 0.0525 Average Nodal Connectivity 2.464 Assortativity Coefficient 0.0717 Fractal dimension 1.8409
Mycelium hyphae network of *Ganoderma lucidum* grown on wood[9].	
	Average Degree 3.1703 Clustering Coefficient 0.0519 Average Nodal Connectivity 2.377 Assortativity Coefficient 0.1709 Fractal Dimension 1.8409

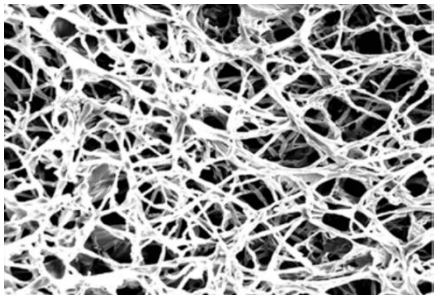
Aspergillus fumigates biofilm grown on confluent layer of human bronchial epithelia cells[10].	
	Average Degree 2.98 Clustering Coefficient 0.067 Average Nodal Connectivity 2.68 Assortativity Coefficient 0.0396 Fractal Dimension 1.8463

Table S2. GT parameters and fractal dimensions for fungal networks shown in Fig. 21.

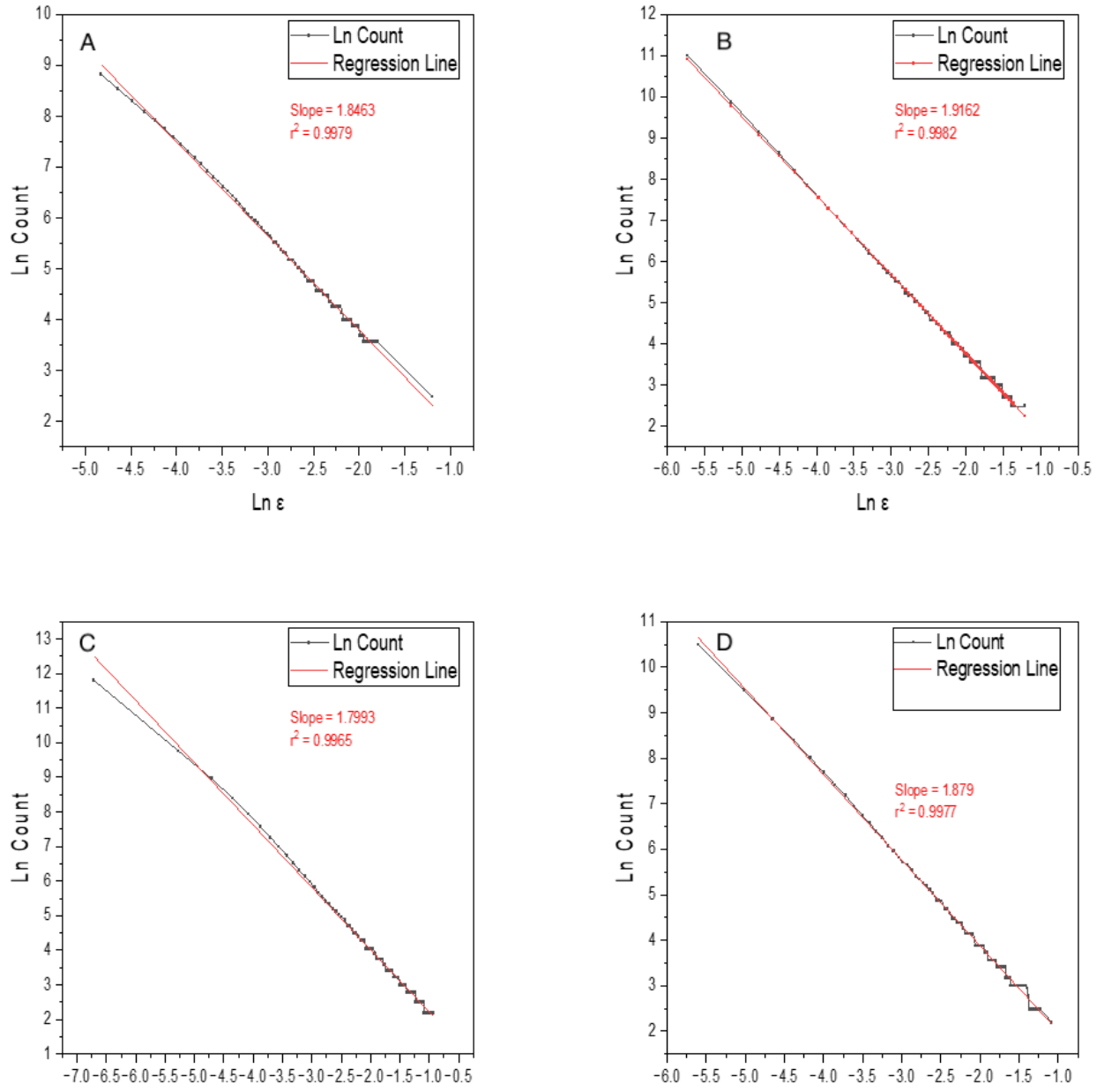
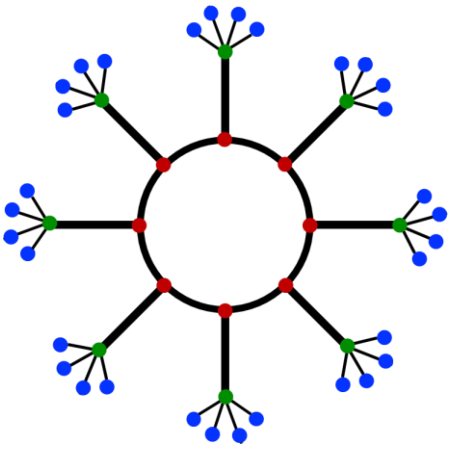


Fig. S22: Examples of calculations of fractal dimensions, d_f. (**A**) *Aspergillus fumigates* biofilm grown on confluent layer of human bronchial epithelia cells[10]. (**B**) *Streptococcus spp.* on agar. (**C**) Self-replicating NPs. (**D**) *R. stolonifera* grown on *Capsicum annuum L.*

Calculation of Complexity Index using GT Model of Hedgehog Particles



5

$$CI_{\bullet} = \bullet + \frac{2\bullet + 1\bullet}{2^1} + \frac{2\bullet + 2\bullet + S\bullet}{2^2} + \frac{2\bullet + 2\bullet + 2S\bullet}{2^3} + \frac{2\bullet + 2\bullet + 2S\bullet}{2^4} + \ldots$$

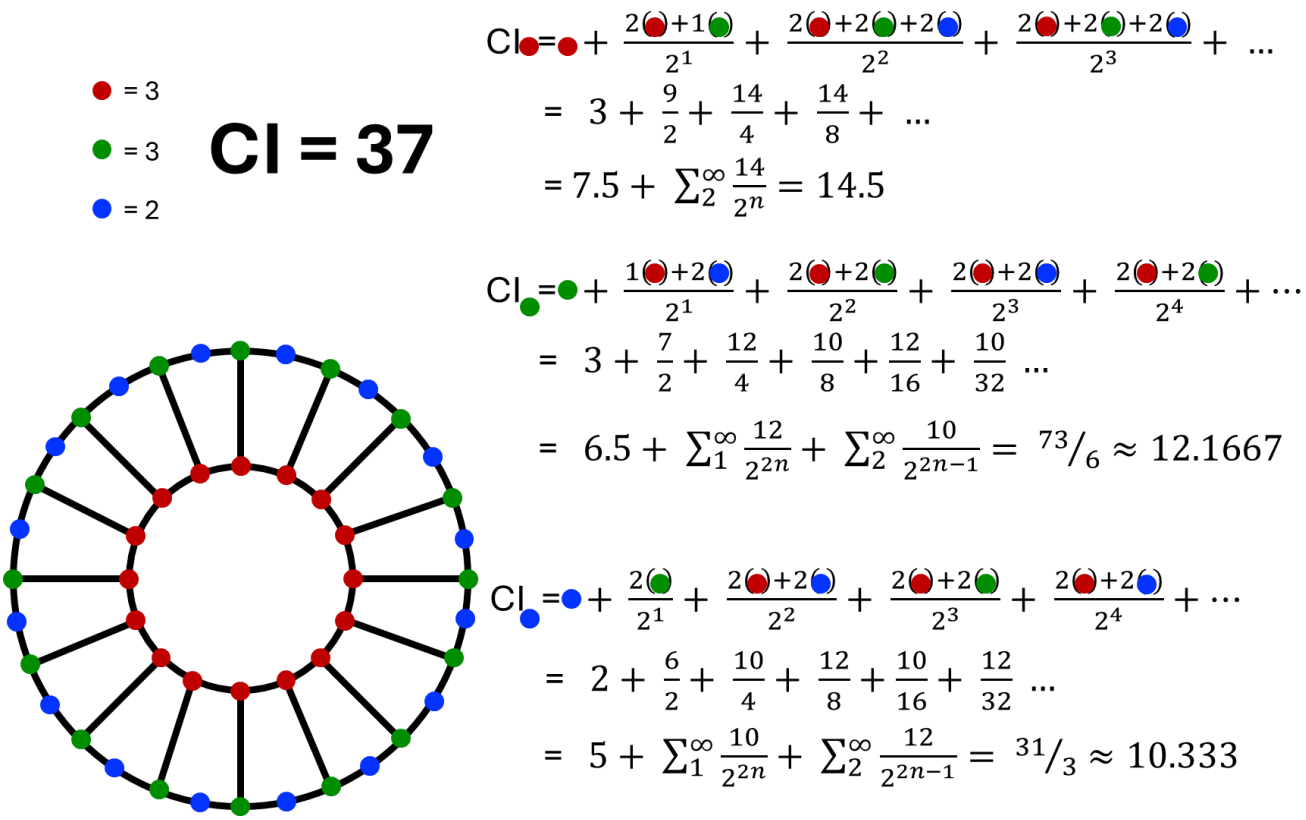
$$= 3 + \frac{S+7}{2} + \frac{3S+8}{4} + \frac{4S+8}{8} + \frac{4S+8}{16} + \ldots$$

$$= \frac{5S+34}{4} + \sum_{n=3}^{\infty} \frac{4S+8}{2^n}$$

For S = 4:
$CI_{\bullet}$ = 19.5

For S = 5:
$CI_{\bullet}$ = 21.75

For S = 6:
$CI_{\bullet}$ = 24



MOVIES

Movie S1.
Dark-field microscopy of self-replicating NPs.

Movie S2.
In-situ liquid-state TEM video of nucleation and growth of NP chains.

Movie S3.
In-situ liquid-state TEM video of nuclei forming at interface of NPs.

Movie S4.
In-situ liquid-state TEM video of NP nucleation and growth under non-replicating synthesis.

SUPPLEMENTARY REFERENCES

(1) Decher, G. Fuzzy Nanoassemblies: Toward Layered Polymeric Multicomposites. *Science* **1997**, *277* (5330), 1232–1237. https://doi.org/10.1126/science.277.5330.1232.

(2) Wilson, E. A. K.; Kumar, P.; Montjoy, D. G.; Kotov, N. A. Dispersion of Hydrophilic "Hedgehog" Microparticles in Liquid CO2 Mixtures. *ACS Nano* **2022**. https://doi.org/10.1021/acsnano.2c03058.

(3) Balamurugan, A.; Kumar, A. Postharvest Fruit Rot of Bell Pepper (Capsicum Annuum L.): Pathogenicity and Host Range of Alternaria Alternata. *Scientia Horticulturae* **2023**, *319*, 112156. https://doi.org/10.1016/j.scienta.2023.112156.

(4) Besson, C.; Finney, E. E.; Finke, R. G. Nanocluster Nucleation, Growth, and Then Agglomeration Kinetic and Mechanistic Studies: A More General, Four-Step Mechanism Involving Double Autocatalysis. *Chem. Mater.* **2005**, *17* (20), 4925–4938. https://doi.org/10.1021/cm050207x.

(5) Thanh, N. T. K.; Maclean, N.; Mahiddine, S. Mechanisms of Nucleation and Growth of Nanoparticles in Solution. *Chem. Rev.* **2014**, *114* (15), 7610–7630. https://doi.org/10.1021/cr400544s.

(6) Völkle, C. M.; Gebauer, D.; Cölfen, H. High-Resolution Insights into the Early Stages of Silver Nucleation and Growth. *Faraday Discuss.* **2015**, *179* (0), 59–77. https://doi.org/10.1039/C4FD00269E.

(7) Ahmadian, M.; Tyson, J. J.; Peccoud, J.; Cao, Y. A Hybrid Stochastic Model of the Budding Yeast Cell Cycle. *npj Syst Biol Appl* **2020**, *6* (1), 1–10. https://doi.org/10.1038/s41540-020-0126-z.

(8) Olivares-Marin, I. K.; González-Hernández, J. C.; Regalado-Gonzalez, C.; Madrigal-Perez, L. A. Saccharomyces Cerevisiae Exponential Growth Kinetics in Batch Culture to Analyze Respiratory and Fermentative Metabolism. *JoVE* **2018**, No. 139, e58192. https://doi.org/10.3791/58192.

(9) De Yoreo, J. A Perspective on Multistep Pathways of Nucleation. In *Crystallization via Nonclassical Pathways Volume 1: Nucleation, Assembly, Observation & Application*; ACS Symposium Series; American Chemical Society, 2020; Vol. 1358, pp 1–17. https://doi.org/10.1021/bk-2020-1358.ch001.

(10) Cheng, Y.; Tao, J.; Zhu, G.; Soltis, J. A.; Legg, B. A.; Nakouzi, E.; De Yoreo, J. J.; Sushko, M. L.; Liu, J. Near Surface Nucleation and Particle Mediated Growth of Colloidal Au Nanocrystals. *Nanoscale* **2018**, *10* (25), 11907–11912. https://doi.org/10.1039/C8NR03408G.

(11) Molleman, B. Skimming the Surface: A Surface Structural Approach to Understanding Silver Ion Release from Silver Nanoparticles., Wageningen University, Wageningen.

(12) Rumptz, J. R.; Mao, Z.; Campbell, C. T. Size-Dependent Adsorption and Adhesion Energetics of Ag Nanoparticles on Graphene Films on Ni(111) by Calorimetry. *ACS Catal.* **2022**, *12* (5), 2888–2897. https://doi.org/10.1021/acscatal.1c05589.

(13) Plessow, P. N.; Campbell, C. T. Influence of Adhesion on the Chemical Potential of Supported Nanoparticles as Modeled with Spherical Caps. *ACS Catal.* **2022**, *12* (4), 2302–2308. https://doi.org/10.1021/acscatal.1c04633.

(14) *Structural Analysis of Nanoscale Network Materials Using Graph Theory | ACS Nano*. https://pubs.acs.org/doi/10.1021/acsnano.1c04711 (accessed 2024-02-13).

(15) Müller, F.-M. C.; Seidler, M.; Beauvais, A. Aspergillus Fumigatus Biofilms in the Clinical Setting. *Medical Mycology* **2011**, *49* (Supplement_1), S96–S100. https://doi.org/10.3109/13693786.2010.502190.
(16) Jones, M.; Bhat, T.; Kandare, E.; Thomas, A.; Joseph, P.; Dekiwadia, C.; Yuen, R.; John, S.; Ma, J.; Wang, C.-H. Thermal Degradation and Fire Properties of Fungal Mycelium and Mycelium - Biomass Composite Materials. *Scientific Reports* **2018**, *8* (1), 17583. https://doi.org/10.1038/s41598-018-36032-9.
(17) Javadian, A.; Ferrand, H. L.; Hebel, D. E.; Saeidi, N. Application of Mycelium-Bound Composite Materials in Construction Industry: A Short Review. *SOJ Materials Science & Engineering* **2020**.
(18) Wuren, T.; Toyotome, T.; Yamaguchi, M.; Takahashi-Nakaguchi, A.; Muraosa, Y.; Yahiro, M.; Wang, D.-N.; Watanabe, A.; Taguchi, H.; Kamei, K. Effect of Serum Components on Biofilm Formation by Aspergillus Fumigatus and Other Aspergillus Species. *Japanese Journal of Infectious Diseases* **2014**, *67* (3), 172–179. https://doi.org/10.7883/yoken.67.172.